

# Analytical Kinematic Model and RCM Control of a Parallel-Serial Steady-Hand Eye Robot

Botao Zhao<sup>1</sup>, Mojtaba Esfandiari<sup>1\*</sup>, Teng Long<sup>1</sup>, Yub Heo<sup>1</sup>,

Peter Gehlbach<sup>2</sup>, Peter Kazanzides<sup>1</sup>, and Iulian Iordachita<sup>1</sup>,

1- Laboratory for Computational Sensing and Robotics,

Johns Hopkins University, Baltimore, MD, 21218, USA,

(E-mail: bzhao17, mesfand2, tlong29, yheo1, pkaz, iordachita@jhu.edu)

2- Wilmer Eye Institute, Johns Hopkins School of Medicine, Baltimore, MD, 21287, USA,

(E-mail: pgelbach@jhmi.edu)

*Maintaining a precise remote center of motion is essential for safe and accurate tool manipulation in retinal microsurgery. However, existing numerical Jacobian identification methods for parallel manipulators often exhibit nonlinear, workspace-dependent inaccuracies and require frequent recalibration, limiting their reliability and clinical applicability. To address these challenges, this study presents an analytical kinematic framework for a hybrid parallel–serial robot designed for retinal surgery, known as the Steady-Hand Eye Robot (SHER 3.0). Closed-form solutions for forward and inverse kinematics, as well as analytical formulations of the direct and inverse Jacobians, are derived to ensure consistent motion estimation across the workspace. The kinematic performance of SHER 3.0 is analyzed to evaluate the manipulability and workspace efficiency. Building on these models, a model predictive control strategy is implemented on SHER 3.0, which maintains the remote center of motion constraint at the sclerotomy with sub-millimeter accuracy, with a root mean square error of  $0.55 \pm 0.12$  mm, in a pilot study on a teleportation experiment. Experimental results demonstrate the effectiveness of the proposed analytical models and control framework in enhancing robot motion stability and robustness of the controller in maintaining the remote center of motion constraints, enabling safe robot-assisted retinal microsurgery.*

## 1 INTRODUCTION

Parallel manipulators (PMs) have attracted significant attention from both researchers and industry because of their distinct advantages over serial robot manipulators [1]. Given that their end-effector is supported by multiple kinematic chains, these systems exhibit superior structural rigidity and dynamic performance while maintaining a lower overall inertia [2]. PMs offer additional benefits such as simplified design and reduced manufacturing costs, while providing high precision and payload, even at high velocities [3]. They have found applications across a variety of fields, including pick-and-place operations [4], robotic legged landers [5], manufacturing [6], and machine tools [7], and medical robotics for surgical [8] and rehabilitation purposes [9].

Focusing on medical robotics for ophthalmic surgeries, several parallel [10] or serial [11] robotic manipulators have been developed that enable manipulation of a surgical instrument inside the eye, provide micromillimeter scale positioning accuracy, and remove hand tremor while satisfying a remote center of motion (RCM) constraint at the sclerotomy to avoid damaging the eye [12, 13]. For example, Micron is a handheld micromanipulator that can filter out physiological hand tremor [14]. Its handheld version, however, lacked RCM enforcement capability because of insufficient degrees of freedom. To address this limitation, an upgraded Micron system incorporating a six-degree-of-freedom (6-DOF) piezoelectric Stewart-platform architecture was later developed [15]. Despite this advancement, Micron remains constrained

---

\*Corresponding author: Mojtaba Esfandiari  
(E-mail: mesfand2@jhu.edu)

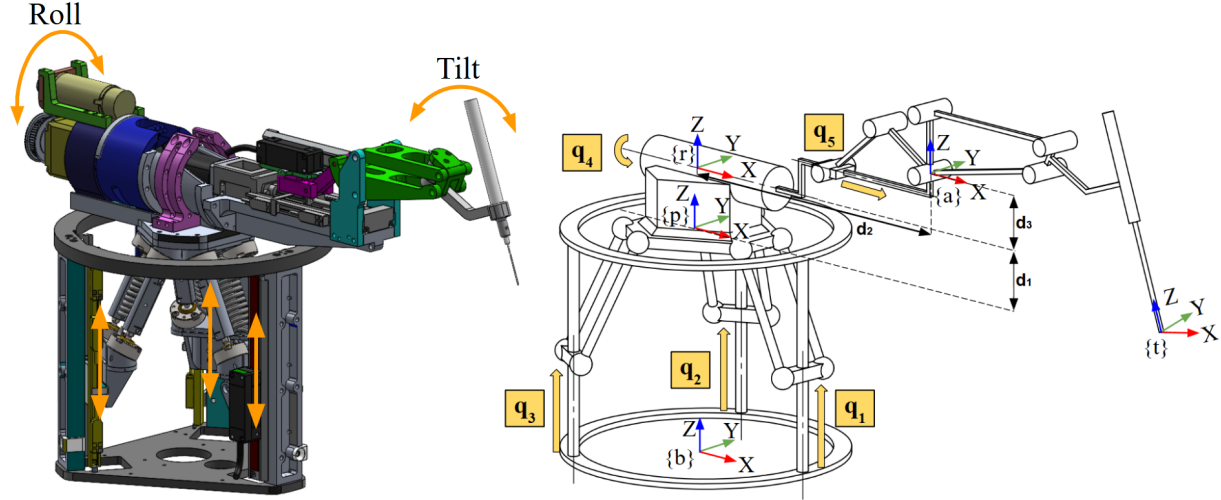


Fig. 1: The CAD model (left) and schematic diagram of the SHER 3.0 kinematic (right).

to a fixed one-to-one force feedback ratio, a characteristic that may be suboptimal for the delicate force requirements of vitreoretinal surgical procedures.

The Steady-Hand Eye Robots (SHERs) [16] are 5-DOF manipulators, developed at Johns Hopkins University for retinal microsurgery applications. They come with several versions having different mechanical designs, including serial and parallel mechanisms [17]. SHER 1 employs a slider–crank mechanism to produce the instrument’s tilt motion [18]. Because this mechanism cannot mechanically enforce a remote center of motion (RCM), a virtual RCM (V-RCM) must be achieved through control and optimization strategies. Other versions of SHER, namely SHER 2.0 and SHER 2.1, are serial manipulators with a translation accuracy of  $5 \pm 2 \mu\text{m}$  for tip position regulation independently along X, Y, and Z Cartesian coordinate axes in free space [19]. These versions employ a parallelogram six-bar mechanism, capable of enforcing RCM in the plane of tilt motion; however, general enforcement of the RCM constraint (restricting lateral out-of-plane motions around the trocar point) still requires V-RCM enforcement via optimization and a control algorithm. Previous studies developed a scleral force-based RCM enforcement using an adaptive force control algorithm and fiber Bragg grating (FBG)-based force-sensing instruments, for bimanual cooperative [20] and bimanual teleoperation [21] frameworks using SHERs 2.0 and 2.1. This method safely minimizes the scleral forces and dynamically enforces the RCM constraint, despite eye and/or head movements; however, it requires advanced FBG-based force-sensing needles, which could have limitations for clinical use. The latest version of this

robot, SHER 3.0 (Fig. 1), is a hybrid robot comprising a linear parallel Delta platform with a serial roll–tilt mechanism [22]. SHER 3.0 adopts a four-bar linkage architecture that is optimized to reduce the linear travel required by the linear Delta stage when implementing a V-RCM during surgical tool tilting [23, 24].

The linear Delta manipulator provides high translational stiffness, low moving inertia, and a compact structure, which are advantageous for precise and stable RCM-constrained motion in eye surgery. The springs in Fig. 1-a are utilized to preload the ball-joint bearings to minimize clearance. The two rotational degrees of freedom, roll and tilt (Fig. 1), reflect the natural manipulation of surgeons during retinal procedures. Axial rotation of the tool is generally not required and is thus omitted from the design. It is worth noting that SHER 3.0 does not have a mechanically enforced RCM; instead, the RCM is enforced virtually through a control algorithm. This is because SHER 3.0 was originally designed as a cooperative surgical robot, and a mechanically enforced RCM was not required. However, the development of a teleoperative control mode requires an RCM enforcement for patient safety. Therefore, this work presents a virtual RCM enforcement by developing analytical kinematics relations and a model predictive control (MPC) implementation, enabling safe tool-to-eye interaction.

Accurate position control of SHER 3.0 is important since retinal surgery operations typically require micromillimeter-scale manipulation accuracy. For example, microsurgical procedures such as subretinal injection require tool tip positioning accuracy of about 25–30  $\mu\text{m}$  [12]. Having an accurate kinematic model is an

essential step to achieve repeatable and consistent position control accuracy; however, as opposed to serial manipulators, kinematic modeling and calibration of parallel mechanisms are challenging tasks [25]. A previous study employed a numerical method for kinematic calibration of SHER 3.0 using the Bernstein polynomial. The root mean square error (RMSE) of the robot position regulation about the X, Y, and Z axes in the tool tip coordinate  $\{t\}$  (Fig. 1) in free space varied from  $23 \pm 1 \mu\text{m}$  to  $121 \pm 80 \mu\text{m}$  at different positions of the robot workspace (at  $Z = -20, 0, 20 \text{ mm}$  in the frame  $\{p\}$  of Fig. 1) [26]. This shows that the accuracy of numerical kinematic calibration methods may not remain consistent across different locations within the SHER 3.0 workspace, due to nonlinear kinematic nature of its parallel mechanism. To reduce this variability in the robot positioning accuracy, the authors in [26] repeated this calibration procedure at multiple regions of interest (ROI) in the end-effectors' local coordinate, achieving an RMSE of less than  $20 \mu\text{m}$  with small variations at different locations of the robot workspace. This method requires repeated calibration at multiple ROIs, which is a challenging and time-consuming procedure.

To resolve these limitations and gaps in science, in this study, we developed analytical models for forward and inverse kinematics and the Jacobian of the parallel robot for retinal microsurgery, the SHER 3.0, and designed a model predictive control algorithm based on these models that accurately satisfies an RCM constraint at the eye sclerotomy. The target operational workspace is defined by the patient's eyeball, which has an approximate diameter of 24 mm, and serves as the primary region of interest for evaluation.

The contributions of this work are listed as follows:

1. We developed analytical models for the forward and inverse kinematics as well as forward and inverse Jacobians, for a parallel-serial robot manipulator, SHER 3.0, for retinal microsurgery applications. We evaluated the kinematics performance of the SHER 3.0, using several kinematic-related metrics such as reachable and dexterous workspace analysis and manipulability index.
2. We implemented an MPC algorithm, using the proposed analytical kinematics and Jacobian models to enforce an RCM constraint that satisfies the clinical precision needed for retinal microsurgeries. We developed a teleoperation framework to evaluate the accuracy and performance of the kinematic models and the MPC controller for SHER 3.0 (integrated with a straight gripper tool attached to its end-effector) in maintaining the RCM constraint in an artificial eye

phantom with a trocar constraint.

3. We increased the dexterity of SHER 3.0 by integrating the Improved Integrated Robotic Intraocular Snake ( $I^2RIS$ ) [27] at its end effector, allowing the surgical tool to achieve a more optimal approach angle to the retinal surface (eye phantom) compared to the straight gripper tool.

The remaining sections of this paper are as follows. Section 2 explains the methodologies in robot kinematics and control. Section 3 presents the experimental setup and procedure. Experimental results are presented in Section 4 and discussed in Section 5. Section 6 concludes the paper.

## 2 MATERIALS AND METHODS

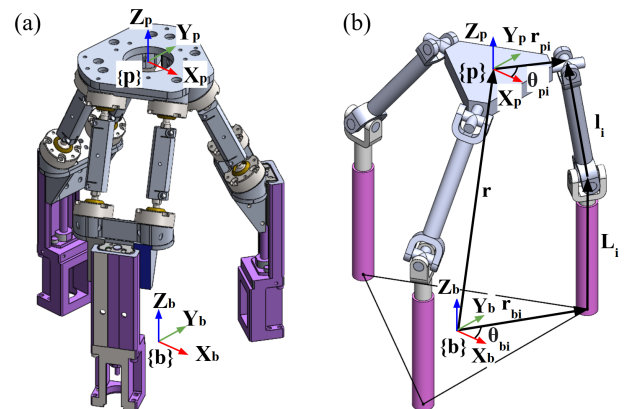


Fig. 2: linear Delta platform: (a) 3D view of the mechanical structure; (b) simplified kinematic model

### 2.1 Forward Kinematics

The proposed eye surgical robot can be decomposed into two serially connected subsystems: a linear parallel delta mechanism and a roll-tilt four-bar mechanism mounted on the moving platform. This decomposition allows the forward kinematics to be derived for each subsystem separately, and the complete forward kinematics of the robot is then obtained by combining these two results. The derivation for the parallel delta mechanism kinematics follows the approach described in [28].

#### 2.1.1 Linear Delta Platform

Fig. 2a shows the linear Delta mechanism, which consists of a base platform, a moving platform, and three

limbs, each formed by two parallel rods connected by spherical joints. This parallelogram configuration constrains the moving platform to pure translational motion by maintaining link parallelism and suppressing torsional deformation. For kinematic modeling, Fig. 2b shows a simplified mechanism with universal joints, as described in [26]. The base and platform joint circle radii are denoted by  $r_b$  and  $r_p$ . The fixed base frame  $\{b\}$  is defined with its  $Z_b$ -axis aligned with the common direction of the three prismatic joints of the linear Delta platform. The projections of the three universal joint centers onto the  $X_bY_b$  plane form an equilateral triangle centered at the origin of the base frame. The configuration in Fig. 2b is for illustrative purposes only. In the implemented design, the positive  $X_b$ -axis is aligned with the first projected joint centers, and the planar angles  $\theta_{bi} \in \{0, \frac{2\pi}{3}, \frac{4\pi}{3}\}$ , where  $i = 1, 2, 3$ , are measured counterclockwise from the  $X_b$ -axis to each projected joint center. The moving platform frame  $\{p\}$  is defined with axes parallel to  $\{b\}$ , and the joint centers are defined in the  $X_pY_p$  plane with angles  $\theta_{pi} \in \{0, \frac{2\pi}{3}, \frac{4\pi}{3}\}$  relative to the  $X_p$  axis. The link length between universal joints is  $l$ , with the corresponding link vector  $\mathbf{l}_i = [x_{li}, y_{li}, z_{li}]^T$ , and the prismatic joint vector  $\mathbf{L}_i = [0, 0, q_i]^T$ . The moving platform position vector is denoted by  $\mathbf{r} = [r_x, r_y, r_z]^T$ . With the above parameters, the  $i$ -th vector loop equation is:

$$\mathbf{l}_i = -\mathbf{L}_i - \mathbf{r}_{bi} + \mathbf{r} + \mathbf{r}_{pi} \quad (1)$$

where

$$\begin{aligned} \mathbf{r}_{bi} &= [r_b \cos \theta_{bi}, r_b \sin \theta_{bi}, 0]^T \\ \mathbf{r}_{pi} &= [r_p \cos \theta_{pi}, r_p \sin \theta_{pi}, 0]^T \end{aligned}$$

let  $\mathbf{e}_i = \mathbf{L}_i + \mathbf{r}_{bi} - \mathbf{r}_{pi}$  and rewrite Eq.(1) as

$$\mathbf{l}_i = \mathbf{r} - \mathbf{e}_i \quad (2)$$

Taking the dot product of Eq.(2) with itself on both sides:

$$\mathbf{l}_i^T \mathbf{l}_i = (\mathbf{r} - \mathbf{e}_i)^T (\mathbf{r} - \mathbf{e}_i) \quad (3)$$

which can be expanded into the scalar form:

$$l^2 = \mathbf{r}^T \mathbf{r} - 2\mathbf{r}^T \mathbf{e}_i + \mathbf{e}_i^T \mathbf{e}_i \quad (4)$$

From Eq.(4), three scalar equations can be written for  $i = 1, 2, 3$  as

$$\begin{aligned} l^2 &= \mathbf{r}^T \mathbf{r} - 2\mathbf{r}^T \mathbf{e}_1 + \mathbf{e}_1^T \mathbf{e}_1 \\ l^2 &= \mathbf{r}^T \mathbf{r} - 2\mathbf{r}^T \mathbf{e}_2 + \mathbf{e}_2^T \mathbf{e}_2 \\ l^2 &= \mathbf{r}^T \mathbf{r} - 2\mathbf{r}^T \mathbf{e}_3 + \mathbf{e}_3^T \mathbf{e}_3 \end{aligned} \quad (5)$$

Pairwise subtraction of these equations, and combine like terms:

$$\begin{aligned} 0 &= -2\mathbf{r}^T (\mathbf{e}_2 - \mathbf{e}_1) + (\mathbf{e}_2^T \mathbf{e}_2 - \mathbf{e}_1^T \mathbf{e}_1) \\ 0 &= -2\mathbf{r}^T (\mathbf{e}_3 - \mathbf{e}_1) + (\mathbf{e}_3^T \mathbf{e}_3 - \mathbf{e}_1^T \mathbf{e}_1) \end{aligned} \quad (6)$$

$$\text{Let } h_1 = \frac{\mathbf{e}_2^T \mathbf{e}_2 - \mathbf{e}_1^T \mathbf{e}_1}{2}, \quad h_2 = \frac{\mathbf{e}_3^T \mathbf{e}_3 - \mathbf{e}_1^T \mathbf{e}_1}{2}$$

Eq.(6) can be written as:

$$\begin{aligned} \mathbf{r}^T (\mathbf{e}_2 - \mathbf{e}_1) - h_1 &= 0 \\ \mathbf{r}^T (\mathbf{e}_3 - \mathbf{e}_1) - h_2 &= 0 \end{aligned} \quad (7)$$

Since all of the elements in  $(\mathbf{e}_2 - \mathbf{e}_1)$  and  $(\mathbf{e}_3 - \mathbf{e}_1)$  are constants, let

$$\begin{aligned} \mathbf{e}_2 - \mathbf{e}_1 &= [x_{21}, y_{21}, z_{21}]^T \\ \mathbf{e}_3 - \mathbf{e}_1 &= [x_{31}, y_{31}, z_{31}]^T \end{aligned}$$

Then Eq.(7) can be expressed as:

$$\begin{aligned} x_{21}r_x + y_{21}r_y + z_{21}r_z - h_1 &= 0 \\ x_{31}r_x + y_{31}r_y + z_{31}r_z - h_2 &= 0 \end{aligned} \quad (8)$$

Rearranging Eq.(8):

$$\begin{aligned} r_x &= \frac{(y_{31}z_{21}/y_{21} - z_{31})}{(x_{31} - y_{31}x_{21}/y_{21})} r_z + \frac{(h_2 - y_{31}h_1/y_{21})}{(x_{31} - y_{31}x_{21}/y_{21})} \\ r_y &= \frac{(x_{31}z_{21}/x_{21} - z_{31})}{(y_{31} - x_{31}y_{21}/x_{21})} r_z + \frac{(h_2 - x_{31}h_1/x_{21})}{(y_{31} - x_{31}y_{21}/x_{21})} \end{aligned} \quad (9)$$

Let

$$\begin{aligned} k_1 &= \frac{(y_{31}z_{21}/y_{21} - z_{31})}{(x_{31} - y_{31}x_{21}/y_{21})}, \quad k_2 = \frac{(h_2 - y_{31}h_1/y_{21})}{(x_{31} - y_{31}x_{21}/y_{21})} \\ k_3 &= \frac{(x_{31}z_{21}/x_{21} - z_{31})}{(y_{31} - x_{31}y_{21}/x_{21})}, \quad k_4 = \frac{(h_2 - x_{31}h_1/x_{21})}{(y_{31} - x_{31}y_{21}/x_{21})} \end{aligned}$$

Then substituting Eq.(9) into the first row of Eq.(5), where  $\mathbf{e}_1 = [e_{1x}, e_{1y}, e_{1z}]^T$ :

$$l^2 = [k_1 r_z + k_2, k_3 r_z + k_4, r_z] \begin{bmatrix} k_1 z + k_2 \\ k_3 z + k_4 \\ r_z \end{bmatrix} - 2 [k_1 r_z + k_2, k_3 r_z + k_4, r_z] \begin{bmatrix} e_{1x} \\ e_{1y} \\ e_{1z} \end{bmatrix} + \mathbf{e}_1^T \mathbf{e}_1 \quad (10)$$

Let

$$T_1 = k_1^2 + k_3^2 + 1$$

$$T_2 = k_1 k_2 + k_3 k_4 - e_{1x} k_1 - e_{1y} k_3 - e_{1z}$$

$$T_3 = k_2^2 + k_4^2 - 2e_{1x} k_2 - 2e_{1y} k_4 - l^2 + e_{1x}^2 + e_{1y}^2 + e_{1z}^2$$

Rearranging Eq.(10):

$$r_z = \frac{-T_2 \pm \sqrt{T_2^2 - T_1 T_3}}{T_1} \quad (11)$$

Since the moving platform must be above the base plane, only positive  $r_z$  solution is valid.

Thus, Eq.(9) and Eq.(11) form the forward kinematic solution  $\mathbf{r} = [r_x, r_y, r_z]^T$  of the linear delta platform. The homogeneous transformation matrix from base frame  $\{b\}$  to platform frame  $\{p\}$  is:

$$T_{bp} = \begin{bmatrix} \mathbf{I}_{3 \times 3} & \mathbf{r}_{3 \times 1} \\ \mathbf{0}_{1 \times 3} & 1 \end{bmatrix} \quad (12)$$

where  $\mathbf{I}_{3 \times 3}$  denotes a  $3 \times 3$  identity matrix,  $\mathbf{r}_{3 \times 1}$  is the position vector of the moving platform, and  $\mathbf{0}_{1 \times 3}$  denotes a  $1 \times 3$  zero matrix.

### 2.1.2 Roll-Tilt Mechanism

The roll-tilt mechanism is a two-DOF hybrid kinematic structure where roll motion is provided by a revolute joint and tilt motion is generated by a four-bar mechanism (Fig. 1). As shown in Fig. 3, the control inputs of this mechanism are the roll angle  $\psi$  and the linear actuator stroke length  $s$ . Point  $\mathbf{P}$  is a user-defined point that can be selected at any location along the tool shaft. Due to the nature of the four-bar linkage, the motion of the tool involves both rotation and translation. However, these two motions are kinematically coupled, knowing one uniquely determines the other.

The forward kinematics is relatively straightforward to compute since the lengths of all the links are known. The present derivation extends the approach introduced in [24]. Link  $AB$  is relatively fixed on the shaft of the roll motor, and point  $P$  maintains fixed relative to link  $CD$ . For simplicity, point  $A$  is defined as the origin of the coordinate system. As the stroke length  $s$  is known:

$$x_{AR} = x_{AR_{max}} - s \quad (13)$$

where  $x_{AR_{max}}$  is the max horizontal distance between the origin to the slider, which is known based on the design parameter, and  $z_{AR}$  is also a fixed value, representing the height from the linear guide rail to the frame  $\{a\}$ .

Thus,

$$L_{AR} = \sqrt{x_{AR}^2 + z_{AR}^2} \quad (14)$$

$$\alpha_4 = \text{atan2}(y_{AR}, z_{AR}) \quad (15)$$

As the lengths of  $AQ$  and  $QR$  are known, from the law of cosine:

$$\alpha_3 = \arccos\left(\frac{L_{AR}^2 + L_{AQ}^2 - L_{QR}^2}{2L_{AR}L_{AQ}}\right) \quad (16)$$

Since  $\phi_1$  and  $\phi_2$  are angles with fixed values, and  $\alpha_3, \alpha_4$  are known:

$$\theta_1 = 180^\circ - (\phi_2 + \alpha_3 - \alpha_4) \quad (17)$$

$$\alpha_1 = \phi_1 - \theta_1 \quad (18)$$

Form the law of cosine again:

$$L_{BD} = \sqrt{L_{AB}^2 + L_{DA}^2 - 2L_{AB}L_{DA} \cos(\alpha_1)} \quad (19)$$

$$\beta_1 = \arccos\left(\frac{L_{AB}^2 + L_{BD}^2 - L_{DA}^2}{2L_{AB}L_{BD}}\right) \quad (20)$$

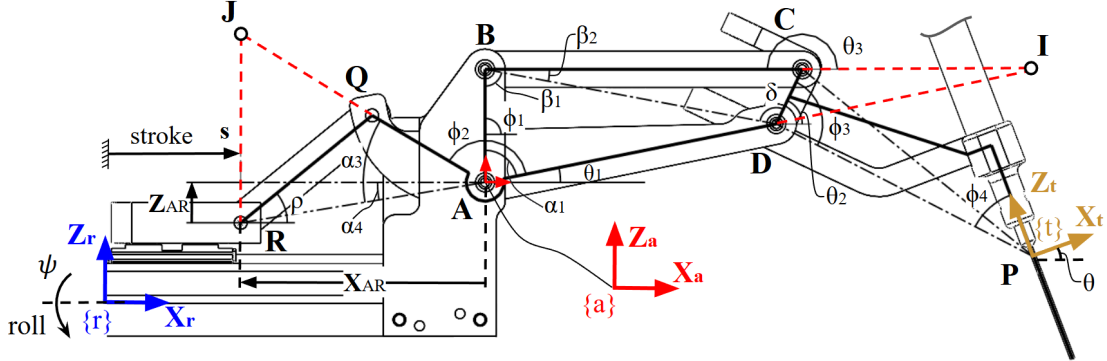


Fig. 3: Side view of the roll–tilt mechanism showing the reference frames and geometric parameters.

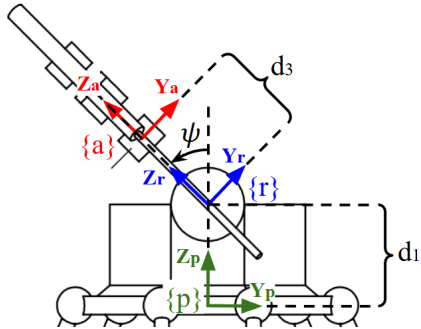


Fig. 4: Simplified front view of the roll-tilt mechanism

$$\delta = \arccos\left(\frac{L_{BD}^2 + L_{CD}^2 - L_{BC}^2}{2L_{BD}L_{CD}}\right) \quad (21)$$

$$\begin{aligned} \theta_2 &= 180^\circ - ((180^\circ - \beta_1 - \phi_1) + \delta) \\ &= \beta_1 + \phi_1 - \delta \end{aligned} \quad (22)$$

Since  $\phi_3$  and  $\phi_4$  are also known and the lengths of  $AD$  and  $DP$  are constants, the  $x$  and  $y$  coordinates of point  $P$  in frame  $\{a\}$  can be directly computed:

$$\begin{aligned} P_x &= \cos(\theta_1)L_{DA} + \cos(\theta_2 - \phi_3)L_{DP} \\ P_z &= \sin(\theta_1)L_{DA} + \sin(\theta_2 - \phi_3)L_{DP} \end{aligned} \quad (23)$$

Let  $\theta = 90^\circ - \phi_4 - (\phi_3 - \theta_2)$ , the angle between the  $x$ -axis of frame  $\{a\}$  and the  $x$ -axis of frame  $\{t\}$ . Then the transformation matrix can be expressed as:

$$T_{at} = \begin{bmatrix} \cos(\theta) & 0 & \sin(\theta) & P_x \\ 0 & 1 & 0 & 0 \\ -\sin(\theta) & 0 & \cos(\theta) & P_z \\ 0 & 0 & 0 & 1 \end{bmatrix} \quad (24)$$

Thus, given the stroke length  $s$ , we can then determine the tool frame's position and orientation relative to frame  $\{a\}$ .

With the transformations  $T_{bp}$  and  $T_{at}$  established, the remaining step to express the tool-tip position and orientation in the base frame  $\{b\}$  is to determine the transformation  $T_{pa}$ .

As illustrated in Fig. 4, the roll angle  $\psi$  is defined with respect to the  $z$ -axis of frame  $\{p\}$ . The roll axis is located a distance  $d_1$  above the linear delta platform frame  $\{p\}$ , while frame  $\{a\}$  is positioned a distance  $d_3$  along the  $z$ -axis of frame  $\{r\}$ . In addition, the displacement between frames  $\{r\}$  and  $\{a\}$  along the  $x$ -axis is  $d_2$ .

Accordingly, the transformation matrices  $T_{pr}$  and  $T_{ra}$  can be written as:

$$\begin{aligned} T_{pr} &= \begin{bmatrix} 1 & 0 & 0 & 0 \\ 0 & \cos(\psi) & -\sin(\psi) & 0 \\ 0 & \sin(\psi) & \cos(\psi) & d_1 \\ 0 & 0 & 0 & 1 \end{bmatrix} \\ T_{ra} &= \begin{bmatrix} 1 & 0 & 0 & d_2 \\ 0 & 1 & 0 & 0 \\ 0 & 0 & 1 & d_3 \\ 0 & 0 & 0 & 1 \end{bmatrix} \end{aligned} \quad (25)$$

Then, by multiplying the two matrices, we obtain the transformation matrix  $T_{pa}$ :

$$\begin{aligned} T_{pa} &= T_{pr}T_{ra} \\ &= \begin{bmatrix} 1 & 0 & 0 & d_2 \\ 0 & \cos(\psi) & -\sin(\psi) & -\sin(\psi)d_3 \\ 0 & \sin(\psi) & \cos(\psi) & \cos(\psi)d_3 + d_1 \\ 0 & 0 & 0 & 1 \end{bmatrix} \end{aligned} \quad (26)$$

Thus, the transformation from base frame  $\{b\}$  to tool

frame  $\{t\}$  is:

$$T_{bt} = T_{bp}T_{pa}T_{at}$$

$$= \begin{bmatrix} \cos(\theta) & 0 & \sin(\theta) & x_{bt} \\ \sin(\theta)\sin(\psi) & \cos(\psi) - \cos(\theta)\sin(\psi) & y_{bt} \\ -\sin(\theta)\cos(\psi) & \sin(\psi) & \cos(\theta)\cos(\psi) & z_{bt} \\ 0 & 0 & 0 & 1 \end{bmatrix} \quad (27)$$

where

$$x_{bt} = P_x + d_2 + r_x$$

$$y_{bt} = -\sin(\psi)P_z - \sin(\psi)d_3 + r_y$$

$$z_{bt} = \cos(\psi)P_z + \cos(\psi)d_3 + d_1 + r_z$$

Since  $\mathbf{r}(q_1, q_2, q_3), \psi(q_4), \theta(q_5), P(q_5)_x, P(q_5)_z$  are all functions of the joint coordinates, this formulation establishes a direct mapping from the configuration space to the task space, thereby defining the forward kinematic model of the serially connected delta and rotation four-bar mechanism.

## 2.2 Inverse Kinematics

Similar to the forward kinematics derivation, the inverse kinematics of each subsystem is derived independently. The results are then combined to form the complete inverse kinematics of the robot.

### 2.2.1 Linear Delta Platform

Write Eq.(1) in matrix form:

$$\begin{bmatrix} l_{ix} \\ l_{iy} \\ l_{iz} \end{bmatrix} = - \begin{bmatrix} 0 \\ 0 \\ q_i \end{bmatrix} - \begin{bmatrix} r_b \cos(\theta_{bi}) \\ r_b \sin(\theta_{bi}) \\ 0 \end{bmatrix} + \begin{bmatrix} r_x \\ r_y \\ r_z \end{bmatrix} + \begin{bmatrix} r_p \cos(\theta_{pi}) \\ r_p \sin(\theta_{pi}) \\ 0 \end{bmatrix} \quad (28)$$

Since the length of each link is  $l = \sqrt{l_{ix}^2 + l_{iy}^2 + l_{iz}^2}$ , Eq.(28) can be written as:

$$l^2 = l_{ix}^2 + l_{iy}^2 + l_{iz}^2$$

$$= (r_x + a_i)^2 + (r_y + b_i)^2 + (r_z - q_i)^2 \quad (29)$$

where

$$a_i = -r_b \cos \theta_{bi} + r_p \cos \theta_{pi}$$

$$b_i = -r_b \sin \theta_{bi} + r_p \sin \theta_{pi}$$

Reorganizing Eq.(29):

$$q_i = r_z - \sqrt{l^2 - (r_x + a_i)^2 - (r_y + b_i)^2} \quad (30)$$

This gives the prismatic actuator extension for each leg, where  $i = 1, 2, 3$ .

### 2.2.2 Roll-Tilt Mechanism

The inverse kinematics of this mechanism presents more complexity. Given the tool tilt angle  $\theta$ , the angle between link  $CD$  and the horizontal axis can be easily obtained as  $\theta_2 = \theta + \phi_3 + \phi_4 - 90^\circ$ . However, substituting  $\theta_2$  back into Eq. (22) to solve for  $\theta_1$  and stroke length  $s$  introduces difficulties, as both  $\beta_1$  and  $\delta$  remain unknown since the length of  $BD$  varies. Solving for these variables would require handling a set of quadratic equations, which can be computationally expensive.

A more efficient approach is to derive the inverse kinematics directly from its geometry by translating edges  $AB$  and  $BC$  to construct a new parallelogram  $ABCE$ , as shown in Figure 5.

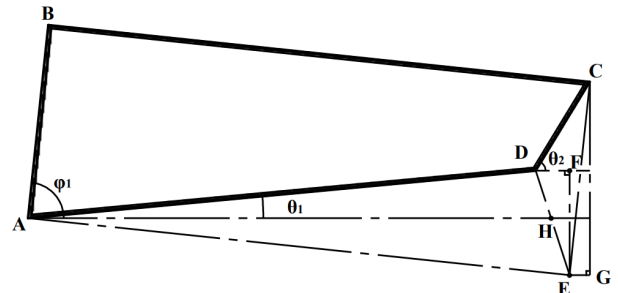


Fig. 5: Close up of the four-bar mechanism

It is obvious to get the following relations:

$$L_{DF} = \cos(\theta_2)L_{CD} - \cos(\phi_1)L_{AB}$$

$$L_{EF} = \sin(\phi_1)L_{AB} - \sin(\theta_2)L_{CD}$$

$$L_{DE} = \sqrt{L_{DF}^2 + L_{EF}^2}$$

Given the lengths of  $AD$ ,  $AE$ , and  $DE$ , using the law of cosine:

$$\angle ADH = \arccos\left(\frac{L_{AD}^2 + L_{DE}^2 - L_{AE}^2}{2L_{AD}L_{DE}}\right)$$

$$\angle AHD = \angle FDH = \arctan(L_{EF}, L_{DF})$$

$$\theta_1 = 180^\circ - \angle ADH - \angle AHD$$

Then, we can use  $\theta_1$  to calculate the stroke length  $s$ .

Let  $\alpha = \alpha_3 + \alpha_4$ :

$$\alpha = 180^\circ - \theta_1 - \phi_2$$

$$x_{AR} = \cos(\alpha)L_{AQ} + \sqrt{L_{QR}^2 - (\sin(\alpha)L_{AQ} - y_{AR})^2}$$

$$s = x_{AR_{max}} - x_{AR}$$

Since the roll angle and stroke length are directly controlled by the revolute and linear actuators, the roll and prismatic joint variables are given by  $\psi = q_4$ ,  $s = q_5$ . This leads to:

$$\begin{aligned} q_4 &= \psi \\ q_5 &= x_{AR_{max}} - x_{AR}(\theta) \end{aligned} \quad (31)$$

where  $\psi$  and  $\theta$  denote the prescribed orientation of the tool.

Given point  $\mathbf{P}$  expressed in frame  $\{a\}$  as  $\mathbf{P}_{\{a\}}$ , its coordinates in the base frame  $\{b\}$ , denoted as  $\mathbf{P}_{\{b\}}$ , can be obtained from Eq.(27):

$$\mathbf{P}_{\{b\}} = \begin{bmatrix} P_{x\{b\}} \\ P_{y\{b\}} \\ P_{z\{b\}} \end{bmatrix} = \begin{bmatrix} P_{x\{a\}} + d_2 + r_x \\ -\sin(\psi)P_{z\{a\}} - \sin(\psi)d_3 + r_y \\ \cos(\psi)P_{z\{a\}} + \cos(\psi)d_3 + d_1 + r_z \end{bmatrix} \quad (32)$$

The base-to-platform vector  $\mathbf{r} = [r_x, r_y, r_z]^T$  is then obtained as:

$$\begin{bmatrix} r_x \\ r_y \\ r_z \end{bmatrix} = \mathbf{P}_{\{b\}} - \begin{bmatrix} P(q_5)_{x\{a\}} + d_2 \\ -\sin(q_4)P(q_5)_{z\{a\}} - \sin(q_4)d_3 \\ \cos(q_4)P(q_5)_{z\{a\}} + \cos(q_4)d_3 + d_1 \end{bmatrix} \quad (33)$$

Then plugging Eq.(33) into Eq.(30) gives the actuator displacements  $q_1, q_2, q_3$ .

Thus, Eq.(30), (31), (33) form the inverse kinematics, proceed as follows: the inputs are the tool position  $\mathbf{P}_{\{b\}}$  and orientation  $(\psi, \theta)$ . From  $\psi$  and  $\theta$ , the joint values  $q_4$  and  $q_5$  are obtained, which in turn determine  $P_{x\{a\}}$  and  $P_{z\{a\}}$ . These allow the computation of  $\mathbf{r}$ , and finally lead to the actuator displacements  $q_1, q_2, q_3$ .

## 2.3 Jacobian

To relate the joint velocities to the tool-tip velocity, the system Jacobian is required. The tool-tip velocity and

the joint velocities are defined as

$$\mathbf{V} = \left[ \dot{x} \ \dot{y} \ \dot{z} \ \dot{\theta}_x \ \dot{\theta}_y \ \dot{\theta}_z \right]_{\{b\}}^T, \quad \dot{\mathbf{q}} = [\dot{q}_1 \ \dot{q}_2 \ \dot{q}_3 \ \dot{q}_4 \ \dot{q}_5]^T$$

Throughout this section, the term Jacobian refers to the spatial Jacobian, where all quantities are expressed in the base frame  $\{b\}$ . The mapping between the joint velocities and the tool-tip velocity is given by

$$\mathbf{V} = \mathbf{J}\dot{\mathbf{q}} \quad (34)$$

where  $\mathbf{J} \in \mathbb{R}^{6 \times 5}$  is the Jacobian matrix. Since  $q_1, q_2, q_3$  only generate translational motions, the upper-left  $3 \times 3$  block of  $\mathbf{J}$  is the Jacobian of the linear delta platform, denoted  $\mathbf{J}_d$ . To find  $\mathbf{J}_d$ , let  $\dot{\mathbf{r}} = [\dot{r}_x, \dot{r}_y, \dot{r}_z]^T$  be the linear delta platform velocity, and  $\dot{\mathbf{l}}_i = [0, 0, \dot{q}_i]^T$  the rate of change of each prismatic joint. Rearranging Eq.(1) and taking derivative of both side:

$$\dot{\mathbf{l}}_i = \dot{\mathbf{r}} - \dot{\mathbf{l}}_i - \dot{\mathbf{r}}_{bi} + \dot{\mathbf{r}}_{pi} \quad (35)$$

Since all of the elements in  $\mathbf{r}_{bi}$  and  $\mathbf{r}_{pi}$  are constants,  $\dot{\mathbf{r}}_{bi} = \dot{\mathbf{r}}_{pi} = 0$ . Thus,

$$\begin{aligned} \dot{\mathbf{l}}_i &= \dot{\mathbf{r}} - \dot{\mathbf{l}}_i \\ &= \dot{\mathbf{r}} - (\omega_i \times \mathbf{l}_i) \end{aligned} \quad (36)$$

Taking the dot product of both sides with  $\mathbf{l}_i$ :

$$\mathbf{l}_i \cdot \dot{\mathbf{l}}_i = \mathbf{l}_i \cdot \dot{\mathbf{r}} - \mathbf{l}_i \cdot (\omega_i \times \mathbf{l}_i) \quad (37)$$

Since  $\mathbf{l}_i$  is perpendicular to  $\omega_i \times \mathbf{l}_i$ :

$$\mathbf{l}_i^T \dot{\mathbf{l}}_i = \mathbf{l}_i^T \dot{\mathbf{r}} \quad (38)$$

$$\begin{bmatrix} l_{ix} & l_{iy} & l_{iz} \end{bmatrix} \begin{bmatrix} 0 \\ 0 \\ \dot{q}_i \end{bmatrix} = \begin{bmatrix} l_{ix} & l_{iy} & l_{iz} \end{bmatrix} \begin{bmatrix} \dot{r}_x \\ \dot{r}_y \\ \dot{r}_z \end{bmatrix} \quad (39)$$

$$l_{iz}\dot{q}_i = l_{ix}\dot{r}_x + l_{iy}\dot{r}_y + l_{iz}\dot{r}_z \quad (40)$$

expand Eq.(40) with  $i = 1, 2, 3$ :

$$\begin{bmatrix} l_{1z} & 0 & 0 \\ 0 & l_{2z} & 0 \\ 0 & 0 & l_{3z} \end{bmatrix} \begin{bmatrix} \dot{q}_1 \\ \dot{q}_2 \\ \dot{q}_3 \end{bmatrix} = \begin{bmatrix} l_{1x} & l_{1y} & l_{1z} \\ l_{2x} & l_{2y} & l_{2z} \\ l_{3x} & l_{3y} & l_{3z} \end{bmatrix} \begin{bmatrix} \dot{r}_x \\ \dot{r}_y \\ \dot{r}_z \end{bmatrix} \quad (41)$$

Thus we can obtain:

$$\dot{\mathbf{r}} = \mathbf{J}_D \dot{\mathbf{q}} \quad (42)$$

where

$$\mathbf{J}_D = \begin{bmatrix} l_{1x} & l_{1y} & l_{1z} \\ l_{2x} & l_{2y} & l_{2z} \\ l_{3x} & l_{3y} & l_{3z} \end{bmatrix}^{-1} \begin{bmatrix} l_{1z} & 0 & 0 \\ 0 & l_{2z} & 0 \\ 0 & 0 & l_{3z} \end{bmatrix} \quad (43)$$

is the  $3 \times 3$  Jacobian matrix of the linear delta platform.

The kinematic contributions of  $q_4$  and  $q_5$  require more careful consideration. As discussed previously, the four-bar linkage introduces coupled motion: actuation of  $q_5$  generates both translation and rotation, while  $q_4$  also contributes to the linear velocity due to the tool tip being offset from its axis of rotation.

Taking derivative of Eq.(23) gives the linear velocity of the tool tip:

$$\begin{aligned} \dot{P}_x &= -\sin(\theta_1)L_{DA}\dot{\theta}_1 - \sin(\theta_2 - \phi_3)L_{DP}\dot{\theta}_2 \\ \dot{P}_z &= \cos(\theta_1)L_{DA}\dot{\theta}_1 + \cos(\theta_2 - \phi_3)L_{DP}\dot{\theta}_2 \end{aligned} \quad (44)$$

Although the velocity relations can be obtained by differentiating the loop-closure equations, the expressions for  $\dot{\theta}_1$  and  $\dot{\theta}_2$  involve derivatives of arctan and arccos functions, which lead to algebraically tedious forms. Thus, the instantaneous center of velocity (ICV) method is used because it yields a more compact and geometrically intuitive closed-form expression, which simplifies implementation and improves code readability. The principle is that, at any given instant, a rigid body in planar motion can be treated as a pure rotation about a unique point in space, referred to as its instantaneous center. For the four-bar mechanism, the center is denoted as point **I**, and for the slider-crank loop, the center is denoted as point **J**, as illustrated in Fig. 3a.

For example, at any instant, link **QR** can be assumed to be in pure rotation with respect to the point **J**, where **QJ** is perpendicular to the velocity of point **Q** and **RJ** is perpendicular to the velocity of point **R**.

Then, from the geometry above:

$$\begin{aligned} L_{JR} &= \tan(\alpha) \cdot x_{AR} - z_{AR} \\ L_{JQ} &= \sec(\alpha) \cdot x_{AR} - L_{AQ} \end{aligned} \quad (45)$$

$$\dot{\rho} = \frac{\dot{s}}{L_{JR}}, \quad L_{AQ} \cdot \dot{\alpha} = -L_{JQ} \cdot \dot{\rho} \quad (46)$$

$$\dot{\theta}_1 = \dot{\alpha} = \frac{L_{JQ}}{L_{AQ} L_{JR}} \dot{s} \quad (47)$$

Similarly, link **CD** can be assumed to be in pure rotation with respect to the point **I**, where **CI** is perpendicular to the velocity of point **C** and **DI** is perpendicular to the velocity of point **D**.

$$\beta_2 = \arccos\left(\frac{L_{BC}^2 + L_{BD}^2 - L_{CD}^2}{2L_{BC}L_{BD}}\right) \quad (48)$$

Let  $\beta = \beta_1 + \beta_2$ :

$$\angle AIB = 180^\circ - \alpha_1 - \beta \quad (49)$$

Then, apply the law of sine:

$$\frac{L_{AB}}{\sin(\angle AIB)} = \frac{L_{IA}}{\sin(\beta)} = \frac{L_{IB}}{\sin(\alpha_1)} \quad (50)$$

Since  $\sin(180^\circ - \alpha_1 - \beta) = \sin(\alpha_1 + \beta)$ :

$$\begin{aligned} L_{IA} &= \frac{L_{AB} \cdot \sin(\beta)}{\sin(\alpha_1 + \beta)} \\ L_{ID} &= L_{IA} - L_{DA} \end{aligned} \quad (51)$$

Using instantaneous center method:

$$\begin{aligned} \dot{\theta}_1 L_{DA} &= -\dot{\theta}_2 L_{ID} \\ \dot{\theta}_2 &= -\frac{L_{DA}}{L_{ID}} \dot{\theta}_1 \end{aligned} \quad (52)$$

From Eq.(47), since  $\dot{\theta}_1 = \frac{L_{JQ}}{L_{AQ} L_{JR}} \dot{s}$ :

$$\dot{\theta}_2 = -\frac{L_{DA} L_{JQ}}{L_{ID} L_{AQ} L_{JR}} \dot{s} \quad (53)$$

Then, plugging Eq.(47) and Eq.(53) into Eq.(44):

$$\begin{aligned}\dot{P}_{x\{a\}} &= \left( -\sin(\theta_1) \frac{L_{DA}L_{JQ}}{L_{AQ}L_{JR}} + \sin(\theta_2 - \phi_3) \frac{L_{DP}L_{DA}L_{JQ}}{L_{ID}L_{AQ}L_{JR}} \right) \dot{s} \\ \dot{P}_{z\{a\}} &= \left( \cos(\theta_1) \frac{L_{DA}L_{JQ}}{L_{AQ}L_{JR}} - \cos(\theta_2 - \phi_3) \frac{L_{DP}L_{DA}L_{JQ}}{L_{ID}L_{AQ}L_{JR}} \right) \dot{s}\end{aligned}\quad (54)$$

Let:

$$\begin{aligned}A &= \left( -\sin(\theta_1) \frac{L_{DA}L_{JQ}}{L_{AQ}L_{JR}} + \sin(\theta_2 - \phi_3) \frac{L_{DP}L_{DA}L_{JQ}}{L_{ID}L_{AQ}L_{JR}} \right) \\ B &= \left( \cos(\theta_1) \frac{L_{DA}L_{JQ}}{L_{AQ}L_{JR}} - \cos(\theta_2 - \phi_3) \frac{L_{DP}L_{DA}L_{JQ}}{L_{ID}L_{AQ}L_{JR}} \right)\end{aligned}$$

This gives a clear and compact expression for the velocity of point  $\mathbf{P}$  as a function of  $\dot{s}$ :

$$\dot{P}_{x\{a\}} = A\dot{s}, \quad \dot{P}_{z\{a\}} = B\dot{s}$$

All velocity components above are respect to frame  $\{a\}$ . According to Figure 3b, the corresponding tool-tip velocity in the linear Delta platform frame  $\{p\}$  can be readily derived as:

$$\begin{bmatrix} \dot{x} \\ \dot{y} \\ \dot{z} \\ \dot{\theta}_x \\ \dot{\theta}_y \\ \dot{\theta}_z \end{bmatrix}_{\{p\}} = \begin{bmatrix} \dot{P}_{x\{a\}} \\ -\sin(\psi)\dot{P}_{z\{a\}} - \cos(\psi)\dot{\psi}(P_{z\{a\}} + d_3) \\ \cos(\psi)\dot{P}_{z\{a\}} - \sin(\psi)\dot{\psi}(P_{z\{a\}} + d_3) \\ \dot{\psi} \\ \cos(\psi)\dot{\theta}_2 \\ \sin(\psi)\dot{\theta}_2 \end{bmatrix} \quad (55)$$

Since  $\dot{\psi} = \dot{q}_4$  and  $\dot{s} = \dot{q}_5$ , Eq.(55) can be written as:

$$\begin{bmatrix} \dot{x} \\ \dot{y} \\ \dot{z} \\ \dot{\theta}_x \\ \dot{\theta}_y \\ \dot{\theta}_z \end{bmatrix}_{\{p\}} = \underbrace{\begin{bmatrix} 0 & A \\ -\cos(q_4)(P_{z\{a\}} + d_3) & -\sin(q_4)B \\ -\sin(q_4)(P_{z\{a\}} + d_3) & \cos(q_4)B \\ 1 & 0 \\ 0 & \cos(q_4) \frac{L_{DA}L_{JQ}}{L_{ID}L_{AQ}L_{JR}} \\ 0 & \sin(q_4) \frac{L_{DA}L_{JQ}}{L_{ID}L_{AQ}L_{JR}} \end{bmatrix}}_{\mathbf{J}_{RT}} \begin{bmatrix} \dot{q}_4 \\ \dot{q}_5 \end{bmatrix} \quad (56)$$

Because there is no rotation between the base frame  $\{b\}$  and the linear delta platform frame  $\{p\}$ , the velocity of the tool tip expressed in  $\{b\}$  is simply the sum of the linear delta platform's velocity in  $\{b\}$  and the tool tip's velocity in fixed  $\{p\}$  frame. This provides all the necessary components for assembling the spatial Jacobian:

$$\mathbf{J} = \begin{bmatrix} \mathbf{J}_D & | & \mathbf{J}_{RT} \\ \mathbf{0}_{3 \times 3} & & \end{bmatrix} \quad (57)$$

where  $\mathbf{J}_D \in \mathbb{R}^{3 \times 3}$  is the Jacobian of the linear delta positioning platform, controlled by joints  $q_1$ ,  $q_2$ , and  $q_3$ .  $\mathbf{J}_{RT} \in \mathbb{R}^{6 \times 2}$  is the Jacobian of the roll-tilt mechanism, controlled by joints  $q_4$  and  $q_5$ .

## 2.4 Jacobian Pseudo-Inverse

Since SHER 3.0 is a 5-DOF robot, its Jacobian matrix is rectangular and a true matrix inverse does not exist. Therefore, a Jacobian pseudo-inverse is derived using an analytical formulation. The Jacobian Pseudo-Inverse is defined as:

$$\dot{\mathbf{q}} = \mathbf{J}^\dagger \mathbf{V} \quad (58)$$

where  $\mathbf{J}^\dagger \in \mathbb{R}^{5 \times 6}$  is the Jacobian Pseudo-Inverse matrix. From Eq.(40), the desired platform velocity can be directly related to the corresponding joint velocities as:

$$\dot{q}_i = \frac{l_{ix}}{l_{iz}} \dot{r}_x + \frac{l_{iy}}{l_{iz}} \dot{r}_y + \dot{r}_z \quad (59)$$

Focusing on the linear delta platform, the joint velocities associated with a given linear platform velocity are:

$$\begin{bmatrix} \dot{q}_1 \\ \dot{q}_2 \\ \dot{q}_3 \end{bmatrix}_{\text{delta}} = \begin{bmatrix} \frac{l_{1x}}{l_{1z}} & \frac{l_{1y}}{l_{1z}} & 1 \\ \frac{l_{2x}}{l_{2z}} & \frac{l_{2y}}{l_{2z}} & 1 \\ \frac{l_{3x}}{l_{3z}} & \frac{l_{3y}}{l_{3z}} & 1 \end{bmatrix} \begin{bmatrix} \dot{r}_x \\ \dot{r}_y \\ \dot{r}_z \end{bmatrix} \quad (60)$$

where the coefficient matrix depends on each limb's position vector of the linear delta mechanism. Eq.(60) maps the platform velocities to joint-space velocities for the linear delta stage, defining the top-left block of the inverse Jacobian.

For the roll and tilt mechanism, since the tool tip is not located along their axes of rotation, both roll and tilt introduce linear displacements in addition to their rotational effects. While angular velocities  $\dot{\theta}_x$ ,  $\dot{\theta}_y$ ,  $\dot{\theta}_z$  will cause nonzero  $\dot{x}$ ,  $\dot{y}$ ,  $\dot{z}$ , these induced translations can be determined analytically, and these induced velocities can be compensated by subtracting them from the linear delta platform velocities. The translational velocities induced

by the roll-tilt mechanism can be expressed as:

$$\begin{bmatrix} \dot{x} \\ \dot{y} \\ \dot{z} \end{bmatrix}_{\{p\}} = \begin{bmatrix} \dot{P}_{x\{a\}} \\ -\sin(\psi)\dot{P}_{z\{a\}} - \cos(\psi)\dot{\psi}(P_{z\{a\}} + d_3) \\ \cos(\psi)\dot{P}_{z\{a\}} - \sin(\psi)\dot{\psi}(P_{z\{a\}} + d_3) \end{bmatrix} \quad (61)$$

By plugging Eq.(61) into Eq.(60), the joint velocities required to compensate the induced linear motion are:

$$\begin{bmatrix} \dot{q}_1 \\ \dot{q}_2 \\ \dot{q}_3 \end{bmatrix} = \begin{bmatrix} \frac{l_{1x}}{l_{1z}} & \frac{l_{1y}}{l_{1z}} & 1 \\ \frac{l_{2x}}{l_{2z}} & \frac{l_{2y}}{l_{2z}} & 1 \\ \frac{l_{3x}}{l_{3z}} & \frac{l_{3y}}{l_{3z}} & 1 \end{bmatrix} \begin{bmatrix} \dot{x} \\ \dot{y} \\ \dot{z} \end{bmatrix}_{\{p\}} \quad (62)$$

To analyze the contribution of the roll and tilt mechanisms to the induced velocity, Eq.(62) need to be reformulated in terms of the roll and tilt rates  $\dot{\psi}$  and  $\dot{\theta}_2$ . Plugging Eq.(52) into Eq.(44) gives the following expression:

$$\begin{aligned} \dot{P}_{x\{a\}} &= (-\sin(\theta_1)L_{ID} + \sin(\theta_2 - \phi_3)L_{DP})\dot{\theta}_2 \\ \dot{P}_{y\{a\}} &= (\cos(\theta_1)L_{ID} - \cos(\theta_2 - \phi_3)L_{DP})\dot{\theta}_2 \end{aligned} \quad (63)$$

Let:

$$\begin{aligned} C &= -\sin(\theta_1)L_{ID} + \sin(\theta_2 - \phi_3)L_{DP} \\ D &= \cos(\theta_1)L_{ID} - \cos(\theta_2 - \phi_3)L_{DP} \end{aligned} \quad (64)$$

Then

$$\begin{aligned} \dot{P}_{x\{a\}} &= C\dot{\theta}_2 \\ \dot{P}_{z\{a\}} &= D\dot{\theta}_2 \end{aligned} \quad (65)$$

Substituting Eq.(65) into Eq.(61), Eq.(62) becomes:

$$\begin{aligned} \begin{bmatrix} \dot{q}_1 \\ \dot{q}_2 \\ \dot{q}_3 \end{bmatrix} &= \underbrace{\begin{bmatrix} \frac{l_{1x}}{l_{1z}} & \frac{l_{1y}}{l_{1z}} & 1 \\ \frac{l_{2x}}{l_{2z}} & \frac{l_{2y}}{l_{2z}} & 1 \\ \frac{l_{3x}}{l_{3z}} & \frac{l_{3y}}{l_{3z}} & 1 \end{bmatrix}}_{\mathbf{M}_D} \begin{bmatrix} C\dot{\theta}_2 \\ -\sin(\psi)D\dot{\theta}_2 - \cos(\psi)(P_{z\{a\}} + d_3)\dot{\psi} \\ \cos(\psi)D\dot{\theta}_2 - \sin(\psi)(P_{z\{a\}} + d_3)\dot{\psi} \end{bmatrix} \\ &= \underbrace{\begin{bmatrix} \frac{l_{1x}}{l_{1z}} & \frac{l_{1y}}{l_{1z}} & 1 \\ \frac{l_{2x}}{l_{2z}} & \frac{l_{2y}}{l_{2z}} & 1 \\ \frac{l_{3x}}{l_{3z}} & \frac{l_{3y}}{l_{3z}} & 1 \end{bmatrix}}_{\mathbf{M}_D} \begin{bmatrix} 0 \\ -\cos(\psi)(P_{z\{a\}} + d_3) - \sin(\psi)D \\ -\sin(\psi)(P_{z\{a\}} + d_3) \end{bmatrix} \begin{bmatrix} \dot{\psi} \\ \dot{\theta}_2 \end{bmatrix} \end{aligned} \quad (66)$$

From Eq.(55), the tool tip's angular velocities in frame  $\{p\}$  are:

$$\begin{bmatrix} \dot{\theta}_x \\ \dot{\theta}_y \\ \dot{\theta}_z \end{bmatrix}_{\{p\}} = \begin{bmatrix} \dot{\psi} \\ \cos(\psi)\dot{\theta}_2 \\ \sin(\psi)\dot{\theta}_2 \end{bmatrix} \quad (67)$$

Since there's no rotational transformation between base frame  $\{b\}$  and linear delta platform frame  $\{p\}$ ,  $[\dot{\theta}_x, \dot{\theta}_y, \dot{\theta}_z]_{\{p\}}^T = [\dot{\theta}_x, \dot{\theta}_y, \dot{\theta}_z]_{\{b\}}^T$ . From Eq.(67), it's clear that  $\dot{\theta}_y$  and  $\dot{\theta}_z$  are coupled through  $\dot{\psi}$  and  $\dot{\theta}_2$ . In other words, specifying  $\dot{\theta}_y$  determines a unique corresponding  $\dot{\theta}_z$  and vice versa.

Since  $\dot{\psi}$  represents the rotational velocity about the base frame's  $x$  axis, and the relationship between  $\dot{\theta}_y$  and  $\dot{\theta}_2$  has been shown in Eq.(67), substituting  $\dot{\psi} = \dot{\theta}_x$  and  $\dot{\theta}_2 = \frac{1}{\cos(\psi)}\dot{\theta}_y$  into Eq.(66) gives:

$$\begin{aligned} \begin{bmatrix} \dot{q}_1 \\ \dot{q}_2 \\ \dot{q}_3 \end{bmatrix} &= \mathbf{M}_D \begin{bmatrix} \dot{\theta}_x \\ \frac{1}{\cos(\psi)}\dot{\theta}_y \end{bmatrix} \\ &= \begin{bmatrix} \mathbf{M}_D[1,1] & \frac{1}{\cos(\psi)}\mathbf{M}_D[1,2] \\ \mathbf{M}_D[2,1] & \frac{1}{\cos(\psi)}\mathbf{M}_D[2,2] \\ \mathbf{M}_D[3,1] & \frac{1}{\cos(\psi)}\mathbf{M}_D[3,2] \end{bmatrix} \begin{bmatrix} \dot{\theta}_x \\ \dot{\theta}_y \end{bmatrix} \end{aligned} \quad (68)$$

Let

$$\mathbf{M}_r = \begin{bmatrix} \mathbf{M}_D[1,1] & \frac{1}{\cos(\psi)}\mathbf{M}_D[1,2] \\ \mathbf{M}_D[2,1] & \frac{1}{\cos(\psi)}\mathbf{M}_D[2,2] \\ \mathbf{M}_D[3,1] & \frac{1}{\cos(\psi)}\mathbf{M}_D[3,2] \end{bmatrix} \quad (69)$$

Then

$$\begin{bmatrix} \dot{q}_1 \\ \dot{q}_2 \\ \dot{q}_3 \end{bmatrix}_{induced} = \mathbf{M}_r \begin{bmatrix} \dot{\theta}_x \\ \dot{\theta}_y \end{bmatrix}_{\{b\}} \quad (70)$$

In this case, it's clear that  $\dot{\theta}_z$  has no effect on  $\dot{q}_1, \dot{q}_2, \dot{q}_3$ . However, to maintain consistency with the full Jacobian inverse expression,  $\dot{\theta}_z$  is included on the right-hand side of Eq.(70), yielding:

$$\begin{bmatrix} \dot{q}_1 \\ \dot{q}_2 \\ \dot{q}_3 \end{bmatrix}_{induced} = [\mathbf{M}_r \ 0] \begin{bmatrix} \dot{\theta}_x \\ \dot{\theta}_y \\ \dot{\theta}_z \end{bmatrix}_{\{b\}} \quad (71)$$

Note that the joint velocities from Eq.(71) represent the linear velocity induced by roll and tilt. In the Jacobian inverse formulation, Eq.(71) is subtracted from Eq.(60) to

eliminate the induced linear velocity.

$$\begin{aligned}
\begin{bmatrix} \dot{q}_1 \\ \dot{q}_2 \\ \dot{q}_3 \end{bmatrix} &= \begin{bmatrix} \dot{q}_1 \\ \dot{q}_2 \\ \dot{q}_3 \end{bmatrix}_{\text{delta}} - \begin{bmatrix} \dot{q}_1 \\ \dot{q}_2 \\ \dot{q}_3 \end{bmatrix}_{\text{induced}} \\
&= \begin{bmatrix} \frac{l_{1x}}{l_{1z}} \frac{l_{1y}}{l_{1z}} 1 \\ \frac{l_{2x}}{l_{2z}} \frac{l_{2y}}{l_{2z}} 1 \\ \frac{l_{3x}}{l_{3z}} \frac{l_{3y}}{l_{3z}} 1 \end{bmatrix} \begin{bmatrix} \dot{x} \\ \dot{y} \\ \dot{z} \end{bmatrix} - [\mathbf{M}_r \ 0] \begin{bmatrix} \dot{\theta}_x \\ \dot{\theta}_y \\ \dot{\theta}_z \end{bmatrix} \\
&= \begin{bmatrix} \frac{l_{1x}}{l_{1z}} \frac{l_{1y}}{l_{1z}} 1 & -\mathbf{M}_{r[1,1]} & -\mathbf{M}_{r[1,2]} & 0 \\ \frac{l_{2x}}{l_{2z}} \frac{l_{2y}}{l_{2z}} 1 & -\mathbf{M}_{r[2,1]} & -\mathbf{M}_{r[2,2]} & 0 \\ \frac{l_{3x}}{l_{3z}} \frac{l_{3y}}{l_{3z}} 1 & -\mathbf{M}_{r[3,1]} & -\mathbf{M}_{r[3,2]} & 0 \end{bmatrix} \begin{bmatrix} \dot{x} \\ \dot{y} \\ \dot{z} \\ \dot{\theta}_x \\ \dot{\theta}_y \\ \dot{\theta}_z \end{bmatrix}_{\{b\}}
\end{aligned} \tag{72}$$

Since  $\dot{\psi} = \dot{\theta}_x = \dot{q}_4$ ,  $\dot{s} = \dot{q}_5$  and  $\dot{\theta}_2 = \frac{1}{\cos(\psi)}\dot{\theta}_y$ , the relationship between  $\dot{q}_5$  and  $\dot{\theta}_y$  can be derived from Eq.(53):

$$\begin{aligned}
\dot{\theta}_2 &= -\frac{L_{DA}L_{JQ}}{L_{ID}L_{AQ}L_{JR}}\dot{s} \\
\frac{1}{\cos(\psi)}\dot{\theta}_y &= -\frac{L_{DA}L_{JQ}}{L_{ID}L_{AQ}L_{JR}}\dot{q}_5 \\
\dot{q}_5 &= -\frac{L_{ID}L_{AQ}L_{JR}}{\cos(q_4)L_{DA}L_{JQ}}\dot{\theta}_y
\end{aligned} \tag{73}$$

Thus, all components needed to construct the Jacobian inverse have been derived. By assembling Eq.(73) with Eq.(72), the joint velocities can be expressed as:

$$\begin{bmatrix} \dot{q}_1 \\ \dot{q}_2 \\ \dot{q}_3 \\ \dot{q}_4 \\ \dot{q}_5 \end{bmatrix} = \begin{bmatrix} \frac{l_{1x}}{l_{1z}} \frac{l_{1y}}{l_{1z}} 1 & -\mathbf{M}_{r[1,1]} & -\mathbf{M}_{r[1,2]} & 0 \\ \frac{l_{2x}}{l_{2z}} \frac{l_{2y}}{l_{2z}} 1 & -\mathbf{M}_{r[2,1]} & -\mathbf{M}_{r[2,2]} & 0 \\ \frac{l_{3x}}{l_{3z}} \frac{l_{3y}}{l_{3z}} 1 & -\mathbf{M}_{r[3,1]} & -\mathbf{M}_{r[3,2]} & 0 \\ 0 & 0 & 0 & 1 \\ 0 & 0 & 0 & 0 \end{bmatrix} - \frac{L_{ID}L_{AQ}L_{JR}}{\cos(q_4)L_{DA}L_{JQ}} \begin{bmatrix} \dot{x} \\ \dot{y} \\ \dot{z} \\ \dot{\theta}_x \\ \dot{\theta}_y \\ \dot{\theta}_z \end{bmatrix} \tag{74}$$

The analytical expression of the spatial Jacobian

Pseudo-Inverse of the SHER 3.0 robot is:

$$\mathbf{J}^\dagger = \begin{bmatrix} \frac{l_{1x}}{l_{1z}} \frac{l_{1y}}{l_{1z}} 1 & -\mathbf{M}_{r[1,1]} & -\mathbf{M}_{r[1,2]} & 0 \\ \frac{l_{2x}}{l_{2z}} \frac{l_{2y}}{l_{2z}} 1 & -\mathbf{M}_{r[2,1]} & -\mathbf{M}_{r[2,2]} & 0 \\ \frac{l_{3x}}{l_{3z}} \frac{l_{3y}}{l_{3z}} 1 & -\mathbf{M}_{r[3,1]} & -\mathbf{M}_{r[3,2]} & 0 \\ 0 & 0 & 0 & 1 \\ 0 & 0 & 0 & 0 \\ 0 & 0 & 0 & -\frac{L_{ID}L_{AQ}L_{JR}}{\cos(q_4)L_{DA}L_{JQ}} 0 \end{bmatrix} \tag{75}$$

## 2.5 Control Strategy

### 2.5.1 Definition of RCM point

In our system, the RCM is defined as a point on the surface of the eyeball. As shown in Fig. 1, the RCM frame is oriented parallel to the base frame, and its origin is located at the center of the insertion site on the eyeball.

### 2.5.2 Model Predictive Control with RCM Constraint

As discussed in the previous section, SHER 3.0 does not have a mechanically enforced RCM. Instead, a virtual RCM constraint is implemented to constrain the robot's motion, and MPC is implemented as the primary control strategy. The system state at time  $t$  is defined by the tool tip pose as:

$$\chi_t = [x, y, z, \theta_x, \theta_y, \theta_z]^T \tag{76}$$

and the system input  $u_t$  at time  $t$  is the joint velocities of the robot:

$$u_t = [\dot{q}_1, \dot{q}_2, \dot{q}_3, \dot{q}_4, \dot{q}_5]^T \tag{77}$$

The cost function is defined as:

$$\begin{aligned}
C = \min \sum_{t=0}^{n-1} & \left[ (\chi_t - \chi_{\text{des}}) Q (\chi_t - \chi_{\text{des}})^T + u_t R u_t^T + l_t D l_t^T \right] \\
& + \chi_n Q_f \chi_n^T
\end{aligned} \tag{78}$$

s.t.

$$\begin{aligned}
\chi_{t+1} &= \chi_t + \mathbf{J}(q_t) u_t dt, \\
q_{t+1} &= q_t + u_t dt, \\
l_t &= \|(p_{\text{rem}} - p) \times \hat{a}_t\|, \\
\dot{\chi}_{\min} &\leq \mathbf{J}(q_t) u_t \leq \dot{\chi}_{\max} \\
\dot{q}_{\min} &\leq u_t \leq \dot{q}_{\max}, \\
Q \succeq 0, R > 0, D \succeq 0, Q_f \succeq 0,
\end{aligned}$$

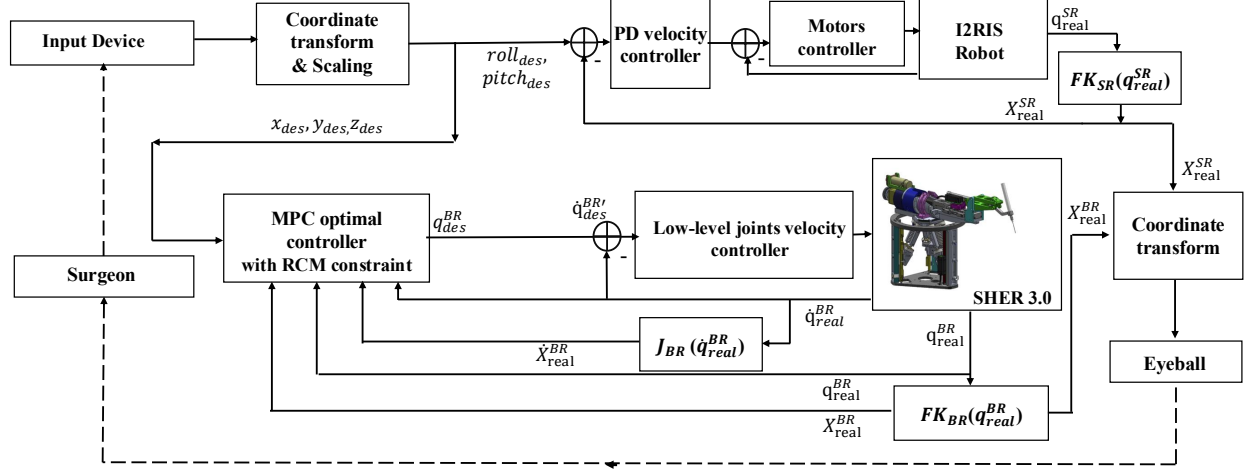


Fig. 6: Control loop diagram of the MPC-based teleoperation control for SHER 3.0

where target end effector state is represented by  $\chi_{des}$ , and  $\mathbf{J}(q_t) \in \mathbb{R}^{6 \times 5}$  represents the Jacobian matrix of the SHER 3.0 system at joint configuration  $q_t$ . The scalar  $l_t$  represents the distance between the gripper shaft and the RCM point, and  $p_{rcm} \in \mathbb{R}^3$  is the position vector of the RCM point,  $p$  refers to the position vector of the straight shaft tip, and  $\hat{a}_t$  indicates the unit vector along the tool shaft direction.

### 2.5.3 Dual Robot Control Loop

In the SHER 3.0 robot control loop, the input device sent the target tool tip position  $x_{des}$ ,  $y_{des}$  and  $z_{des}$  to the MPC optimal controller. The desired values are sent to the optimal controller shown in Eq. 78, which outputs the joint-velocity command  $\dot{q}_{des} \in \mathbb{R}^5$  for SHER 3.0. A motion-limiting block guarantees the safe execution of commanded motions. The limited joint velocity  $\dot{q}'_{des}$  is defined as

$$\dot{q}'_{des} = \begin{cases} E^T \dot{q}_{des}, & \alpha = 1 \\ 0, & \text{otherwise} \end{cases} \quad (79)$$

where  $\alpha$  is a binary indicator. The mapping function  $E \in \mathbb{R}^5$  ( $E_i = 1$  or  $0$ ) restricts motion along allowable directions determined by the translational inputs  $x_{des}, y_{des}, z_{des}$  from the input device and the current  $\dot{\chi}_{real} \in \mathbb{R}^6$  of the tool pose. The resulting target joint velocity  $\dot{q}'_{real} \in \mathbb{R}^5$  is then sent to the low-level velocity controller, which moves the five joints of SHER 3.0. The joint velocity  $\dot{q}_{real}$  is used to update the Jacobian  $\mathbf{J}$  in

Eq. 57 for the next iteration and compute the corresponding Cartesian tip velocity  $\dot{\chi}_{real}$ .

---

#### Algorithm 1 RCM-Constrained Control Algorithm

---

**Require:** Initial joint state  $\mathbf{q}_0$

**Ensure:** Joint velocity command  $\dot{\mathbf{q}}$

- 1:  $\mathbf{q} \leftarrow \mathbf{q}_0$
  - 2: **while** system is enabled **do**
  - 3:    $\mathbf{u}_h \leftarrow$  read input device command
  - 4:    $\mathbf{u}_r \leftarrow \mathcal{T}(\mathbf{u}_h)$  {transform to robot frame}
  - 5:    $\mathbf{u}_r \leftarrow \mathcal{S}(\mathbf{u}_r)$  {scaling}
  - 6:    $\mathbf{T}_{bt} \leftarrow f(\mathbf{q})$  {forward kinematics, Eq. (27)}
  - 7:    $\mathbf{J} \leftarrow J(\mathbf{q})$  {Jacobian, Eq. (57)}
  - 8:    $\dot{\mathbf{q}}_d \leftarrow \text{MPC}(\mathbf{u}_r, \mathbf{q}, \mathbf{J})$  {Eq. (78)}
  - 9:   apply  $\dot{\mathbf{q}}_d$  to joint velocity controller
  - 10:    $\mathbf{q} \leftarrow$  read joint feedback
  - 11: **end while**
- 

Designed specifically for SHER 3.0, the I<sup>2</sup>RIS micromanipulator extends the system with two extra degrees of freedom [29]; however, in our experiment, it is operated as a straight surgical tool. I<sup>2</sup>RIS control loop used single PD control. The input device sent desired orientation  $\theta_{x_{des}}, \theta_{y_{des}}$ , and  $\theta_{z_{des}}$  to the micro manipulator's motors. The target input drives the I<sup>2</sup>RIS to move in different directions.

Fig. 6 shows the detailed control loop diagram for this MPC-based teleoperation controller. To avoid confusion, note that the notations used in the figure differ slightly from those in the main text: *BR* denotes the Base

Robot (SHER 3.0), and  $SR$  denotes the micro manipulator ( $I^2RIS$ ). Algorithm 1 shows the steps of the SHER 3.0 control loop and the relative matched formulas.

### 3 EXPERIMENTS

To evaluate the overall performance of the proposed kinematics and Jacobian models and the MPC-based RCM control algorithm, three distinct experiments were conducted, each targeting a specific goal as follows:

*1-Kinematic Analysis:* To analyze the kinematic performance of SHER 3.0.

*2- RCM Control Evaluation:* To evaluate the performance of the implementation of the MPC control algorithm and analyze the accuracy of the robot kinematics and Jacobian in maintaining the RCM constraint in a teleoperation experiment using SHER 3.0 and a straight gripper tool.

*3-Approach Angle Evaluation:* To evaluate and compare the performance of the  $I^2RIS$  snake robot and the straight gripper tool in providing optimum approach angle to the retina surface while the RCM constraint is maintained by the SHER 3.0 and the MPC controller.

#### 3.1 Experimental Setup

Fig. 7 and 8 illustrate the experimental setup, which includes the SHER 3.0 with a motion controller (Galil, CA, USA) for low-level joint velocity control. A 6-DOF force/torque sensor (Nano17, ATI Industrial Automation, NC, USA) is attached to SHER’s end-effector to measure the forces/torques applied by the user’s hand and to enable cooperative control in an admittance-based strategy [16]. The high-level MPC controller with RCM constraint, mid-level inverse kinematics solver, and low-level joint velocity controller were all implemented in C++ using the CISST-SAW libraries, running at an update rate of 200 Hz [30]. To evaluate the RCM control accuracy, a set of 3-millimeter ArUco markers were rigidly mounted on the robot’s end-effector, tracking its position and orientation using a digital microscope (AD407, Andonstar, China) calibrated using a standard pinhole camera model. A 3D-printed eye phantom with a diameter of 24 mm (typical human eye diameter), incorporates a gimbal joint that functions as the RCM to simulate the sclerotomy. The robotic instrument shaft is inserted through the gimbal joint, simulating the RCM constraint during the eye surgery procedures. A Phantom Omni haptic interface is used for control of the actual SHER 3.0 with a straight gripper tool attached to its end-effector (Fig. 7-a) and their digital twin counterparts in the Asynchronous Multi-Body Framework (AMBF) platform (Fig. 7-b). An

Omega 7 haptic interface is used for teleoperation control of the Improved Integrated Robotic Intraocular Snake ( $I^2RIS$ ) attached to the SHER 3.0 end-effector (Fig. 8).

### 3.2 Experimental Procedures

#### 3.2.1 Kinematic Analysis

The SHER 3.0 kinematic relations are modeled in Python and analyzed based on several kinematics-related metrics, such as reachable and dexterous workspaces, and manipulability index. The reachable and dexterous workspaces are evaluated and presented for the entire SHER 3.0 robot end-effector (linear Delta stage combined with the roll-tilt mechanism). The manipulability index are evaluated and presented for the linear parallel Delta stage and the roll-tilt mechanism separately.

In this work, the dexterous workspace of SHER 3.0 is defined as the subset of the reachable workspace that has more than one inverse kinematic solution. This concept aligns with prior microsurgical robot research [31].

The manipulability of the roll-tilt mechanism and the linear delta platform of SHER 3.0 are evaluated using Yoshikawa’s classical manipulability index [32], which quantifies the isotropy of velocity transmission between joint space and task space. The manipulability index is defined as:

$$w = \sqrt{\det(\mathbf{J}^T \mathbf{J})} \quad (80)$$

where  $\mathbf{J}$  is the Jacobian matrix of the robot, and  $w$  represents the volume of the velocity manipulability ellipsoid, which indicates the ability of the end-effector to generate arbitrary motion directions given bounded joint inputs. A smaller  $w$  corresponds to configurations where the mechanism loses directional controllability. It is worth noting that Yoshikawa’s manipulability index is meaningful only when the task-space variables are homogeneous, i.e., composed solely of translational or solely of rotational quantities. Since SHER 3.0 comprises decoupled translational and rotational subsystems, the manipulability analysis is performed separately for the linear Delta platform and the roll-tilt mechanism. Separate manipulability indices are defined using the corresponding Jacobians from Eq. 57, denoted as  $w_D$  and  $w_{RT}$ , computed from  $\mathbf{J}_D$  and  $\mathbf{J}_{RT}$  as shown below:

$$\begin{aligned} w_D &= \sqrt{\det(\mathbf{J}_D^T \mathbf{J}_D)} \\ w_{RT} &= \sqrt{\det(\mathbf{J}_{RT}^T \mathbf{J}_{RT})} \end{aligned} \quad (81)$$

For the roll-tilt mechanism, although roll is actuated by a

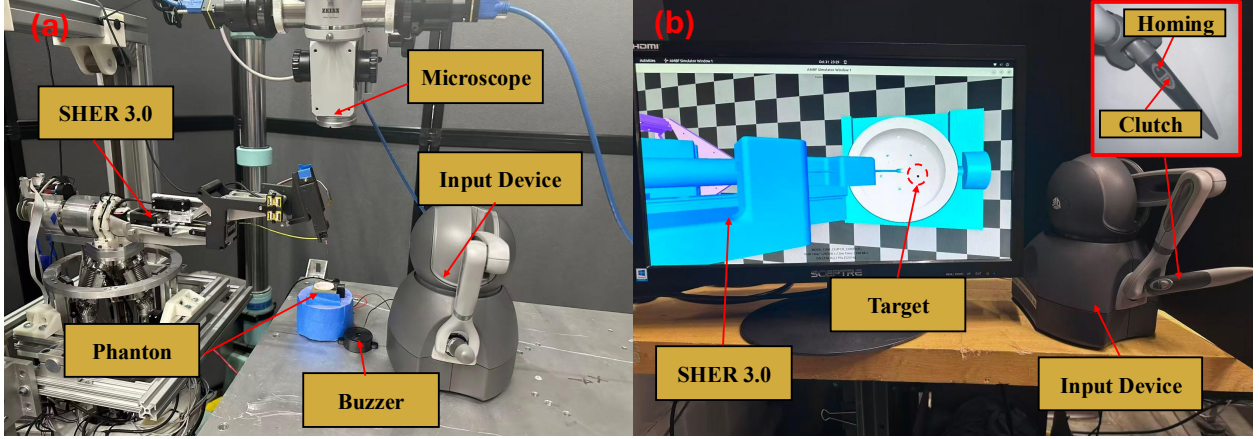


Fig. 7: Experiment setup for the teleoperation system with the SHER 3.0 and a straight gripper tool attached to the end-effector. Actual robots (a) and their digital twin in the AMBF environment (b). The setup also includes a Phantom Omni haptic interface, a surgical microscope, and an eye phantom with a buzzer to confirm touching the target points at the bottom of the phantom with the tool tip.

revolute joint and tilt is produced by a prismatic actuator through a four-bar linkage, these two motions are kinematically independent, and the roll joint does not influence the tilt velocity transmission, as shown in Fig. 13a. Therefore, they are combined in the manipulability analysis. To facilitate interpretation of the manipulability distribution of the roll–tilt and the linear delta mechanism, a normalized manipulability index is introduced here:

$$w_{norm} = \frac{w}{w_{max}} \quad (82)$$

where  $w_{max}$  is the maximum manipulability index within the considered joint and task space.

### 3.2.2 RCM Control Evaluation

To assess the performance of the robot kinematics and the MPC control algorithm in maintaining the RCM constraint, safely and accurately, we conducted a pilot study experiment with five users in a teleportation framework. Before the experiments began, the participants were asked to manipulate the digital twin of the robot using a haptic interface for 5 min, followed by another 5 min manipulation of the actual robot in free space (Figs. 7 and 9) to familiarize themselves with the setup and adjust the seat height, robot position, and microscope focus based on their preference (Fig. 10).

This experiment includes inserting a surgical instrument – a straight gripper tool attached to the SHER 3.0 end-effector – through the trocar into the eye phantom, manipulating the instrument towards a set of target points

(five points selected in a random order), and touching the points with the tool tip (this is considered as one trial). An electrical buzzer is used to confirm the touch. Each participant completed five trials, and the sequence of the target points was identical across all users for consistency. The robot end-effector motion was tracked using two external microscopes and ArUco markers for later analysis of RCM constraint accuracy.

### 3.2.3 Approach Angle Evaluation

It is challenging to approach the retinal surface with an optimum and controllable angle using the straight gripper tool, as it lacks a dexterous wrist-like motion capability, a problem that could be solved by integrating the I<sup>2</sup>RIS snake robot to the SHER 3.0 end-effector. In this experiment, we replaced the straight gripper tool with the I<sup>2</sup>RIS robot, which provides two additional DOFs, pitch and yaw bending angles at the distal end, enabling an optimum approach angle (for example, normal) to the retinal surface. The users were asked to manipulate the SHER 3.0 robot using the Omega 7 haptic interface, move it along the surface of a cylindrical eye phantom to reach 5 reference points along the surface, equally distributed between -20° to 20°. The users were supposed to bend the I<sup>2</sup>RIS robot to keep its tip as perpendicular as possible to the retina surface (see the top row of Fig. 15), while the MPC controller automatically enforces the RCM constraint for the shaft of I<sup>2</sup>RIS robot passing through the trocar (bottom row of Fig. 15).

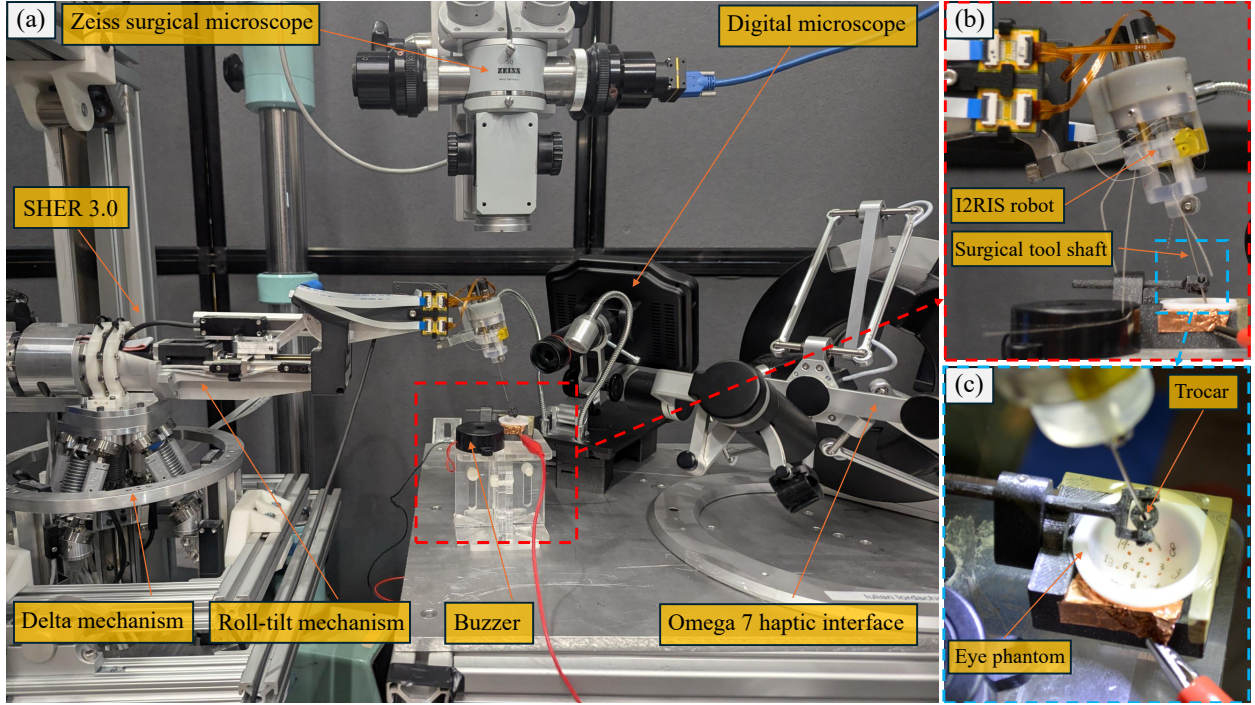


Fig. 8: Experiment setup for the teleoperation system with the SHER 3.0 and a snake-like robot with gripper ( $I^2$ RIS) attached to the end-effector (left). The  $I^2$ RIS robot provides a wrist-like motion with extra DOFs, pitch, and yaw (top right), and its shaft passes through a trocar (creating RCM constraint) to enter the eye phantom (bottom right). The setup also includes an Omega 7 haptic interface, a surgical microscope, and a digital microscope to track the robot end-effector motion (left).

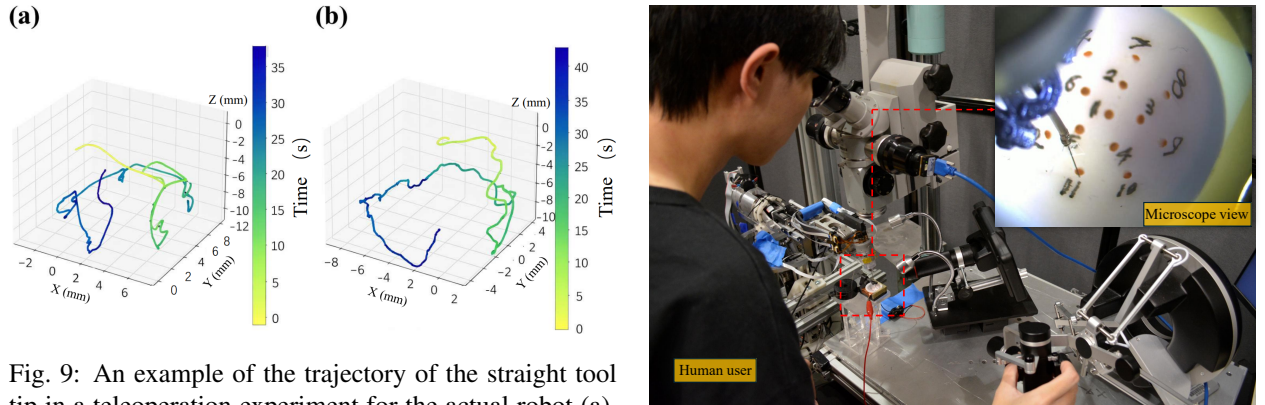


Fig. 9: An example of the trajectory of the straight tool tip in a teleoperation experiment for the actual robot (a), and for that of its digital twin in AMBF (b).

Fig. 10: Experimental procedure.

## 4 RESULTS

This section presents the results using two main approaches: a theoretical approach that performs a kinematic analysis of the SHER 3.0 robot, studying the kinematics performance of the robot mechanism design, followed by an experimental approach that validates the ac-

curacy and performance of the RCM control implementation within a pilot study teleportation experiment with five users.

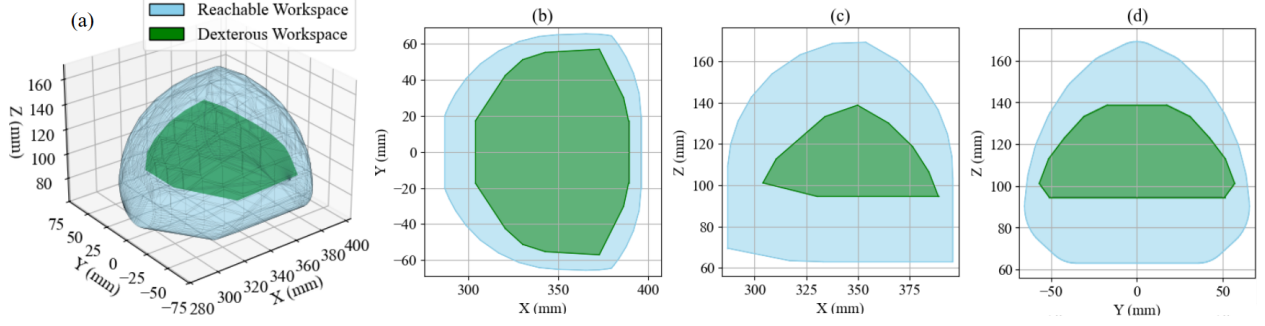


Fig. 11: Reachable and dexterous workspaces of SHER 3.0: (a) 3D view and (b)  $X_bY_b$ , (c)  $X_bZ_b$ , (d)  $Y_bZ_b$  planar views.

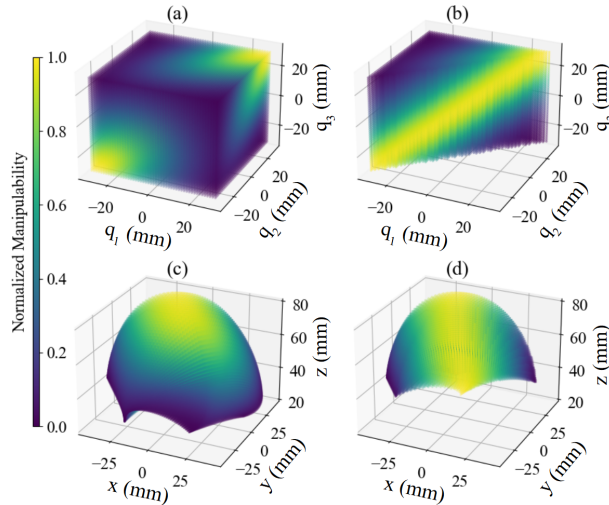


Fig. 12: Normalized manipulability index of the delta platform: (a) distribution in joint space and (c) in task space. Plots (b) and (d) show corresponding 45° cross-sectional views of the joint space and task space, respectively.

## 4.1 Kinematic Analysis

### 4.1.1 Workspace Analysis

The reachable and dexterous workspaces of the tool tip of SHER 3.0 are shown in Fig. 11, expressed in the robot's base frame, which includes the 3D workspaces (Fig. 11-a) and their corresponding 2D projections on the  $X_bY_b$ ,  $X_bZ_b$ , and  $Y_bZ_b$  planes (Figs. 11-b to 11-d). The volumes of the reachable and dexterous workspaces are calculated as  $8.878 \times 10^5 \text{ mm}^3$  and  $1.977 \times 10^5 \text{ mm}^3$ , respectively, with a dexterous-to-reachable ratio of 22.27% as shown in Table 1.

All experiments were conducted within workspace limited by hardware limit switches. For the Delta platform, each limb prismatic actuator was constrained

to a stroke of  $\pm 30 \text{ mm}$ , resulting in the translational workspace shown in Fig. 12-c. The slider crank linear actuator operated over a range of 0 to 50 mm, corresponding to a tool tilt angle of  $109.6^\circ$  to  $159.1^\circ$  between the  $Y_tZ_t$  and  $X_aY_a$  planes. In addition, the tool roll angle was constrained to  $\pm 90^\circ$  between the  $X_tZ_t$  and  $X_pZ_p$  planes.

### 4.1.2 Manipulability Analysis

For the linear delta platform, the normalized manipulability volume in joint space is plotted as functions of the three joint variables  $q_1, q_2, q_3$ , and in task space as a function of the Cartesian coordinates  $x, y, z$  in the base frame, as shown in Fig. 12. As shown in Fig. 12-a and 12-b, the linear delta mechanism has higher manipulability when the three joint values are similar. Correspondingly, Fig. 12-c and 12-d indicate that the region of highest manipulability forms an approximately cylindrical core near the center of the delta's reachable task space.

The maximum, minimum, and mean values of the normalized manipulability index for the linear delta mechanism are 1.0,  $4.4 \times 10^{-5}$  and 0.426 respectively, with a standard deviation of 0.275 as shown in Table 1.

For the roll-tilt mechanism, the normalized manipulability surface is plotted as a function of the two joint variables  $q_4 = \psi$  and  $q_5 = s$ , as shown in Fig. 13. It is observed that the roll-tilt mechanism has its minimum normalized manipulability index around the two near-singular configurations at joint variable  $s \approx 25 \text{ mm}$  and  $s \approx 50 \text{ mm}$ , with corresponding tool angles  $\theta_{tool} = 133.7^\circ$  and  $\theta_{tool} = 159.1^\circ$  (see Figs. 13-b and 13-c).

The maximum, minimum, and mean values of the normalized manipulability index for the roll-tilt mechanism are 1.0, 0.046 and 0.286, respectively, with a standard deviation of 0.205 as shown in Table 1.

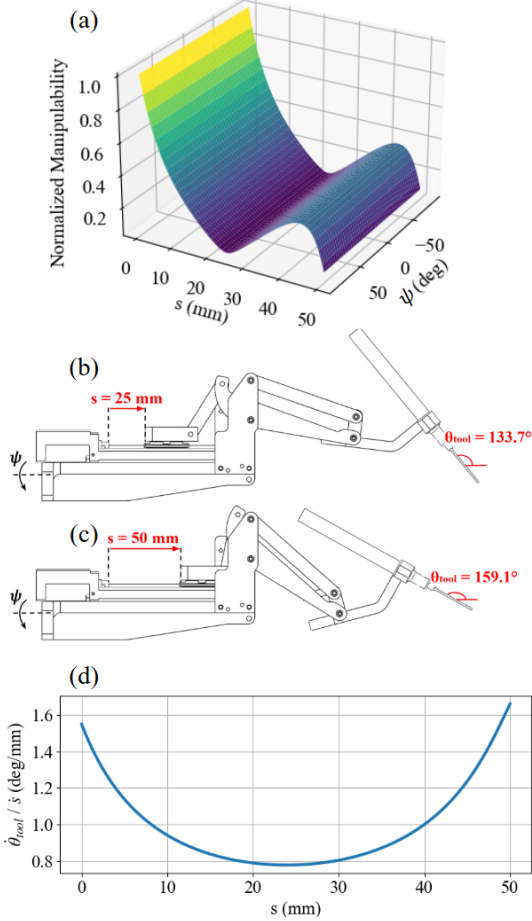


Fig. 13: Normalized manipulability index of the roll-tilt mechanism: (a) overall distribution across the joint space; (b) near-singular configuration at  $s = 25$  mm, with corresponding  $\theta_{tool} = 133.7^\circ$ ; (c) near-singular configuration at  $s = 50$  mm, with corresponding  $\theta_{tool} = 159.1^\circ$ . (d) Tool-to-stroke velocity ratio with stroke length ranging from 0 to 50 mm.

## 4.2 RCM Control Results

Five male users, with ages ranging from 24 to 40 (mean 29.8), participated in this pilot study teleportation experiment. We employed the 10-item Edinburgh Handedness Inventory (EHI) score to evaluate the handedness of the users [33]. All users were dominantly right-handed with a Laterality Quotient (LQ) of  $100.00 \pm 0.00$ . A total of 25 trials are collected from the users, and the results of the accuracy of the RCM control algorithm are summarized in Table 2. Fig. 14 illustrates an example of the trajectory (position and orientation) of the shaft of the straight gripper tool (attached to SHER 3.0 end-effector), which passed through the trocar point on the eye phan-

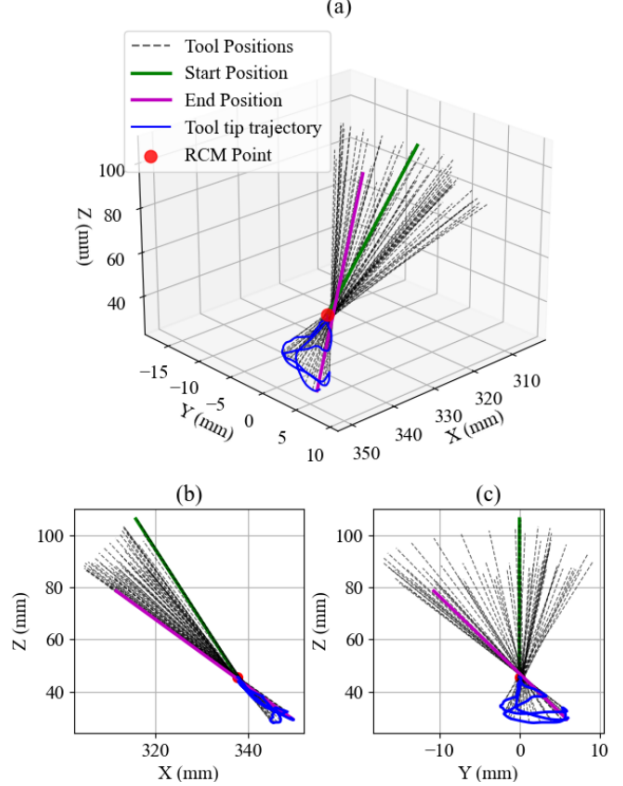


Fig. 14: Visualization of one trial from the RCM experiments: (a) tool tip path with the start and end tool positions highlighted, and (b)  $X_bZ_b$  plane, (c)  $Y_bZ_b$  plane projections.

tom during the teleportation experiments. The blue curve shows the tip trajectory of the surgical tool while touching the target points. The dashed lines represent the footprint of the position/orientation of the tool shaft during a single trial. The RCM error, defined as the distance between the closest point on the axis of the tool shaft to the center of the trocar hole, is measured as  $0.55 \pm 0.12$  mm with a maximum error value of 0.73 mm, which satisfies the clinical requirements for doing a safe robot-assisted manipulation of surgical instruments inside the eye. Of note, the inner diameter of a typical trocar used in retinal surgery is 0.89 mm (20-gauge) [34].

## 4.3 Approach Angle Results

The approach angle of the straight tool gripper and I<sup>2</sup>RIS snake gripper were measured when the gripper was aligned with the reference points. It can be observed that it is challenging to maintain a consistent (close to normal) approach angle using the straight tool, as it varied from  $105.6^\circ$  to  $74.9^\circ$  (see the straight tool in Table 3 and Fig.

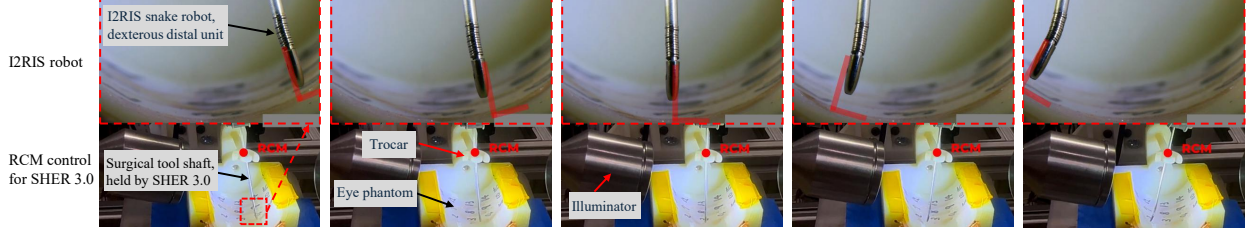


Fig. 15: RCM constraint implementation on SHER 3.0: The shaft of the surgical instrument attached to the SHER 3.0 end-effector pivots through a trocar point (bottom row). The I<sup>2</sup>RIS snake robot, attached to the distal end of the surgical instrument, enables an optimum approach angle (perpendicular in this case) to the retinal surface (top row). Of note, the top row is the magnified view of the I<sup>2</sup>RIS distal end approaching the retina surface of the cylindrical eye phantom in the bottom row.

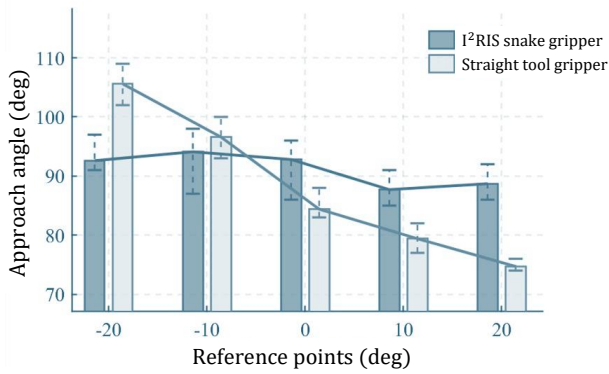


Fig. 16: Comparison of approach angles across five reference points at the bottom of the cylindrical eye phantom: using the I<sup>2</sup>RIS snake robot vs. the straight gripper tool.

16). Conversely, with the use of I<sup>2</sup>RIS snake robot, a relatively consistent approach angle of approximately 90° is observed for all reference points (see the I<sup>2</sup>RIS snake in Table 3 and Fig. 15). This limitation of the straight tool is because the orientation of the tool shaft is constrained at the trocar to satisfy the RCM requirement. The resulting lack of control over the distal approach angle reduces surgical dexterity during procedures such as epiretinal membrane (ERM) peeling, which requires smooth delamination of the membrane along a helical trajectory to minimize hemorrhage. In contrast, the I<sup>2</sup>RIS snake robot enables a wrist-like motion, providing pitch, yaw, and gripping motions that enhance surgeon dexterity and facilitate safer and more efficient ERM peeling.

## 5 DISCUSSION AND FUTURE WORK

The kinematic formulation of the SHER 3.0 robotic system, including the forward and inverse kinematics and

Table 1: Kinematic performance metrics of SHER 3.0. (Delta) and (RT) denote the linear Delta platform and the roll–tilt mechanism.

Metric	Value
Reachable workspace vol. (mm <sup>3</sup> )	8.878 × 10 <sup>5</sup>
Dexterous workspace vol. (mm <sup>3</sup> )	1.977 × 10 <sup>5</sup>
Dexterous-to-reachable ratio	22.27%
Max manipulability (Delta)	2.21
Normalized Min manipulability (Delta)	4.4 × 10 <sup>-5</sup>
Normalized Mean manipulability (Delta)	0.426
Normalized Std. of manipulability (Delta)	0.275
Max manipulability (RT)	39.78
Normalized Min manipulability (RT)	0.046
Normalized Mean manipulability (RT)	0.286
Normalized Std. of manipulability (RT)	0.205

Table 2: Results for the RCM control experiment

Metric	Value
Max. RCM error (mm)	0.73
Min. RCM error (mm)	0.01
Mean RCM error (mm)	0.55
Std. of RCM error (mm)	0.12

their corresponding Jacobian and pseudo-inverse (Eq. 27, Eqs. 30-33, Eq. 57, and Eq. 75), is derived in closed form. This closed-form formulation reduces computational load

and facilitates real-time implementation. The workspace analysis demonstrates that the dexterous workspace of SHER 3.0 is sufficient to cover the target operational region, corresponding to the patient’s eyeball with an approximate diameter of 24 mm. This confirms that the robot can achieve full dexterity within the surgical workspace, enabling flexible tool positioning and orientation during microsurgical procedures. The manipulability analysis shows two notable singularities: at  $s \approx 25$  mm, where the tool-tip velocity is significantly reduced, which is consistent with the discovery in the prior work [24] for this type of tilt mechanism; while at  $s \approx 50$  mm, the mechanism approaches its limit. These findings highlight the regions in which the robot operates with reduced manipulability and can inform safe operational boundaries during surgical tasks.

The RCM error is measured to be  $0.55 \pm 0.12$  mm, with a maximum value of 0.73 mm. This level of error meets clinical safety requirements for robot-assisted intraocular instrument manipulation, as the inner diameter of a standard retinal surgery trocar is approximately 0.89 mm (20-gauge) [34].

Regarding the gripper’s approach angle, the straight tool shows limited controllability over the approach angle at different locations of the retina, due to the RCM constraint enforcement at the trocar, which limits the tool shaft orientation. As such, it is difficult to approach the anatomy at optimal angles for microsurgical procedures such as ERM peeling, which requires smooth delamination of the ERM along a helical trajectory to minimize hemorrhage. The I<sup>2</sup>RIS snake robot allows for additional pitch, yaw, and gripping motions beyond the trocar, at the distal end of the instrument shaft. This wrist-like motion provides surgeons with the necessary dexterity to perform ERM peeling safely and efficiently.

One limitation of this work is the number of users

Table 3: Approach angle of I<sup>2</sup>RIS snake gripper vs. straight tool gripper (mean  $\pm$  std) over five different reference points.

Reference Point	I <sup>2</sup> RIS snake	Straight tool
-20°	$92.6^\circ \pm 1.8$	$105.6^\circ \pm 2.1$
-10°	$94.1^\circ \pm 3.3$	$96.6^\circ \pm 2.3$
0°	$92.8^\circ \pm 3.3$	$84.4^\circ \pm 1.4$
10°	$87.7^\circ \pm 1.8$	$79.4^\circ \pm 1.4$
20°	$88.7^\circ \pm 1.7$	$74.9^\circ \pm 1.0$

(five). This is a pilot study that focuses on the validation of the proposed kinematics models and the feasibility of the SHER 3.0 and I<sup>2</sup>RIS robotic systems and the MPC control algorithm in enforcing the RCM constraint in an artificial eye phantom. Another limitation is that the eye phantom used in this experiment is a 3D-printed component that simulates the RCM constraint at the eye sclerotomy. Still, it has a relatively rigid trocar without sufficient deformability to represent that of human eye sclera tissue. To address these limitations in our future works and to improve experimental realism, we plan to extend the study to multiple users and use biological phantoms, such as ex-vivo porcine eyes, to better mimic the structural and mechanical properties of real tissues, and to further analyze the performance of this robotic system in doing ERM peeling procedures.

## 6 CONCLUSION

This work presents, for the first time, a thorough analytical forward and inverse kinematics and Jacobian models for the SHER 3.0, with a Delta-based parallel-serial mechanism. Based on these analytical models, an MPC algorithm is designed to maintain an RCM constraint at eye sclerotomy during robot-assisted retinal microsurgical procedures. A kinematic analysis is performed to calculate the reachable and dexterous workspaces of the robot. Moreover, the manipulability performance of the SHER 3.0 is evaluated across the robot’s joint space and end-effector task space. Finally, the accuracy of the MPC-based controller in enforcing the RCM constraint is evaluated in a pilot study of a teleportation experiment. Experimental results demonstrate that the proposed kinematics and Jacobian models, together with the MPC control algorithm, satisfy clinical requirements for RCM accuracy, providing a safe and precise robot-assisted retinal surgery platform with robust control performance.

## ACKNOWLEDGEMENTS

This work was supported by the U.S. National Institutes of Health under grant numbers R01EB023943 and R01EB034397, and partially by Johns Hopkins University internal funds.

## CONFLICT OF INTEREST

The authors declare no conflicts of interest.

## DATA AVAILABILITY STATEMENT

The authors attest that all data related to this study are included in the paper.

## REFERENCES

- [1] Taghirad, H. D., 2025, *Parallel robots: mechanics and control* CRC press.
- [2] Müller, A., 2025, “Parallel robots,” *Robotics Goes MOOC: Design*, pp. 89–165.
- [3] Han, G., Xie, F., Liu, X.-J., Meng, Q., and Zhang, S., 2020, “Technology-oriented synchronous optimal design of a 4-degrees-of-freedom high-speed parallel robot,” *Journal of Mechanical Design*, **142**(10), p. 103302.
- [4] Huang, T., Li, Z., Li, M., Chetwynd, D. G., and Gosselin, C. M., 2004, “Conceptual design and dimensional synthesis of a novel 2-dof translational parallel robot for pick-and-place operations,” *J. Mech. Des.*, **126**(3), pp. 449–455.
- [5] Han, Y., and Guo, W., 2022, “A computable framework to efficiently design both current and robotic legged landers for extraterrestrial exploration mission,” *Journal of Mechanical Design*, **144**(1), p. 014501.
- [6] Coppola, G., Zhang, D., Liu, K., and Gao, Z., 2013, “Design of parallel mechanisms for flexible manufacturing with reconfigurable dynamics,” *Journal of mechanical design*, **135**(7), p. 071011.
- [7] Russo, M., Zhang, D., Liu, X.-J., and Xie, Z., 2024, “A review of parallel kinematic machine tools: Design, modeling, and applications,” *International Journal of Machine Tools and Manufacture*, **196**, p. 104118.
- [8] Khalifa, A., Fanni, M., Mohamed, A. M., and Miyashita, T., 2018, “Development of a new 3-dof parallel manipulator for minimally invasive surgery,” *The International Journal of Medical Robotics and Computer Assisted Surgery*, **14**(3), p. e1901.
- [9] Aginaga, J., Iriarte, X., Plaza, A., and Mata, V., 2018, “Kinematic design of a new four degree-of-freedom parallel robot for knee rehabilitation,” *Journal of Mechanical Design*, **140**(9), p. 092304.
- [10] Nakano, T., Sugita, N., Ueta, T., Tamaki, Y., and Mitsuishi, M., 2009, “A parallel robot to assist vitreoretinal surgery,” *International journal of computer assisted radiology and surgery*, **4**(6), pp. 517–526.
- [11] Nasseri, M. A., Eder, M., Nair, S., Dean, E., Maier, M., Zapp, D., Lohmann, C. P., and Knoll, A., 2013, “The introduction of a new robot for assistance in ophthalmic surgery,” In 2013 35th Annual International Conference of the IEEE Engineering in Medicine and Biology Society (EMBC), IEEE, pp. 5682–5685.
- [12] Vander Poorten, E., Riviere, C. N., Abbott, J. J., Bergeles, C., Nasseri, M. A., Kang, J. U., Sznitman, R., Faridpooya, K., and Iordachita, I., 2020, “Robotic retinal surgery,” In *Handbook of robotic and image-guided surgery*. Elsevier, pp. 627–672.
- [13] Dede, M. İ. C., Mobedi, E., and Deniz, M. F., 2025, “A hybrid control scheme for backdriving a surgical robot about a pivot point,” *Robotics*, **14**(10), p. 144.
- [14] MacLachlan, R. A., Becker, B. C., Tabares, J. C., Podnar, G. W., Lobes, L. A., and Riviere, C. N., 2011, “Micron: an actively stabilized handheld tool for microsurgery,” *IEEE transactions on robotics*, **28**(1), pp. 195–212.
- [15] Yang, S., MacLachlan, R. A., and Riviere, C. N., 2014, “Manipulator design and operation of a six-degree-of-freedom handheld tremor-canceling microsurgical instrument,” *IEEE/ASME transactions on mechatronics*, **20**(2), pp. 761–772.
- [16] Üneri, A., Balicki, M. A., Handa, J., Gehlbach, P., Taylor, R. H., and Iordachita, I., 2010, “New steady-hand eye robot with micro-force sensing for vitreoretinal surgery,” In 2010 3rd IEEE RAS & EMBS International Conference on Biomedical Robotics and Biomechatronics, IEEE, pp. 814–819.
- [17] Zhao, B., Esfandiari, M., Usevitch, D. E., Gehlbach, P., and Iordachita, I., 2023, “Human-robot interaction in retinal surgery: A comparative study of serial and parallel cooperative robots,” In 2023 32nd IEEE International Conference on Robot and Human Interactive Communication (RO-MAN), IEEE, pp. 2359–2365.
- [18] Mitchell, B., Koo, J., Iordachita, I., Kazanzides, P., Kapoor, A., Handa, J., Hager, G., and Taylor, R., 2007, “Development and application of a new steady-hand manipulator for retinal surgery,” In Proceedings 2007 IEEE International Conference on Robotics and Automation, IEEE, pp. 623–629.
- [19] Dehghani, S., Sommersperger, M., Zhang, P., Martin-Gomez, A., Busam, B., Gehlbach, P., Navab, N., Nasseri, M. A., and Iordachita, I., 2023, “Robotic navigation autonomy for subretinal injection via intelligent real-time virtual ioct volume slicing,” In IEEE International Conference on Robotics and Automation: ICRA:[proceedings]. IEEE International Conference on Robotics and Automation, Vol. 2023, p. 4724.
- [20] Esfandiari, M., Kim, J. W., Zhang, P., Heng, J. S., Gehlbach, P., Taylor, R. H., and Iordachita, I. I., 2025, “Bimanual robotic eye manipulation using

- adaptive sclera force control: Towards safe retinal vein cannulation,” *IEEE Transactions on Medical Robotics and Bionics*.
- [21] Esfandiari, M., Gehlbach, P., Taylor, R. H., and Iordachita, I. I., 2025, “Bimanual manipulation of steady-hand eye robots with adaptive sclera force control: Cooperative versus teleoperation strategies,” *IEEE transactions on human-machine systems*.
- [22] Alamdar, A., Usevitch, D. E., Wu, J., Taylor, R. H., Gehlbach, P., and Iordachita, I., 2023, “Steady-hand eye robot 3.0: Optimization and benchtop evaluation for subretinal injection,” *IEEE transactions on medical robotics and bionics*, **6**(1), pp. 135–145.
- [23] Wu, J., Li, G., Urias, M., Patel, N. A., Liu, Y.-h., Gehlbach, P., Taylor, R. H., and Iordachita, I., 2020, “An optimized tilt mechanism for a new steady-hand eye robot,” In 2020 IEEE/RSJ International Conference on Intelligent Robots and Systems (IROS), IEEE, pp. 3105–3111.
- [24] Roth, R., Wu, J., Alamdar, A., Taylor, R. H., Gehlbach, P., and Iordachita, I., 2021, “Towards a clinically optimized tilt mechanism for bilateral micromanipulation with steady-hand eye robot,” In 2021 International Symposium on Medical Robotics (ISMR), IEEE, pp. 1–7.
- [25] Karmakar, S., and Turner, C. J., 2024, “A literature review on stewart–gough platform calibrations,” *Journal of Mechanical Design*, **146**(8), p. 083302.
- [26] Xiao, B., Alamdar, A., Song, K., Ebrahimi, A., Gehlbach, P., Taylor, R. H., and Iordachita, I., 2022, “Delta robot kinematic calibration for precise robot-assisted retinal surgery,” In 2022 International Symposium on Medical Robotics (ISMR), IEEE, pp. 1–7.
- [27] Esfandiari, M., Zhou, Y., Dehghani, S., Hadi, M., Munawar, A., Phalen, H., Usevitch, D. E., Gehlbach, P., and Iordachita, I., 2024, “A data-driven model with hysteresis compensation for i 2 ris robot,” In 2024 International Symposium on Medical Robotics (ISMR), IEEE, pp. 1–7.
- [28] Li, Y., and Xu, Q., 2005, “Kinematic analysis and dynamic control of a 3-puu parallel manipulator for cardiopulmonary resuscitation,” In ICAR’05. Proceedings., 12th International Conference on Advanced Robotics, 2005., IEEE, pp. 344–351.
- [29] Jinno, M., and Iordachita, I., 2021, “Improved integrated robotic intraocular snake: Analyses of the kinematics and drive mechanism of the dexterous distal unit,” *Journal of medical robotics research*, **6**(01n02), p. 2140001.
- [30] Deguet, A., Kumar, R., Taylor, R., and Kazanzides, P., 2008, “The cisst libraries for computer assisted intervention systems,” In MICCAI Workshop on Systems and Arch. for Computer Assisted Interventions, Midas Journal, Vol. 71.
- [31] Hoshayarmanesh, H., Zareinia, K., Lama, S., and Sutherland, G. R., 2021, “Structural design of a microsurgery-specific haptic device: neuroarm-plushd prototype,” *Mechatronics*, **73**, p. 102481.
- [32] Yoshikawa, T., 1985, “Manipulability of robotic mechanisms,” *The international journal of Robotics Research*, **4**(2), pp. 3–9.
- [33] Oldfield, R. C., 1971, “The assessment and analysis of handedness: the edinburgh inventory,” *Neuropsychologia*, **9**(1), pp. 97–113.
- [34] Mohamed, S., Claes, C., and Tsang, C. W., 2017, “Review of small gauge vitrectomy: progress and innovations,” *Journal of ophthalmology*, **2017**(1), p. 6285869.